Nucleic Acids Research, 2025, **53**, gkaf816
https://doi.org/10.1093/nar/gkaf816
Gene regulation, Chromatin and Epigenetics

A direct interaction between the Chd1 CHCT domain and Rtf1 controls Chd1 distribution and nucleosome positioning on active genes

Sarah A. Tripplehorn [1,†], Santana M. Lardo [1,†], Margaret K. Shirra [1], Hannah G. Marvil [1], Sarah J. Hainer [1,2,*], Karen M. Arndt [1,*]

[1]Department of Biological Sciences, University of Pittsburgh, Pittsburgh, PA, 15260, United States
[2]UPMC Hillman Cancer Center, University of Pittsburgh, Pittsburgh, PA, 15232, United States

[*]To whom correspondence should be addressed. Email: arndt@pitt.edu
Correspondence may also be addressed to Sarah J. Hainer. Email: sarah.hainer@pitt.edu
[†]The first two authors should be regarded as Joint First Authors.

Abstract

The nucleosome remodeler Chd1 is required for the re-establishment of nucleosome positioning in the wake of transcription elongation by RNA Polymerase II. Previously, we found that Chd1 occupancy on gene bodies depends on the Rtf1 subunit of the Paf1 complex in yeast. Here, we identify an N-terminal region of Rtf1 and the CHCT domain of Chd1 as sufficient for their interaction and demonstrate that this interaction is direct. Mutations that disrupt the Rtf1–Chd1 interaction result in an accumulation of Chd1 at the 5′ ends of Chd1-occupied genes, increased cryptic transcription, altered nucleosome positioning, and concordant shifts in histone modification profiles. We show that a homologous region within mouse RTF1 interacts with the CHCT domains of mouse CHD1 and CHD2. This work supports a conserved mechanism for coupling Chd1 family proteins to the transcription elongation complex and identifies a cellular function for a domain within Chd1 about which little is known.

Graphical abstract

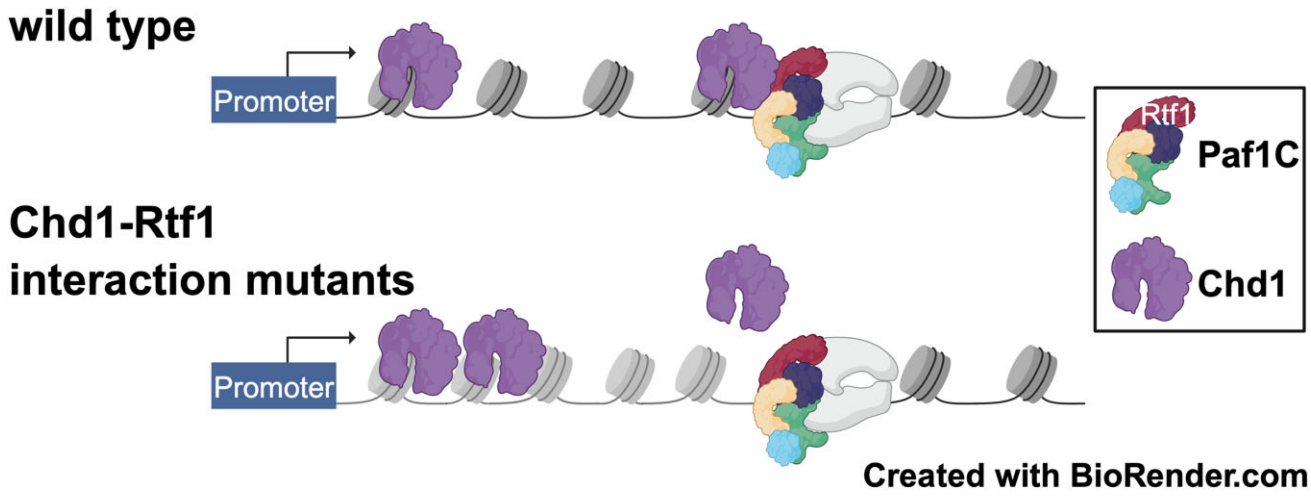

Introduction

Accurate transcription by RNA Polymerase II (RNA Pol II) requires the regulated alteration of nucleosomes both for access to the underlying DNA sequence and maintenance of chromatin structure. Nucleosomes are repositioned, ejected, or compositionally altered by nucleosome remodeling enzymes in coordination with the transcription cycle and other nuclear events [1, 2]. First discovered through genetic screens in *Saccharomyces cerevisiae*, nucleosome remodelers have now been identified in many eukaryotes, and a wealth of information from biochemical and structural studies has provided elegant insights into their modes of catalysis [1, 2]. Despite these advances, we lack a full understanding of how nucleosome remodelers function *in vivo* and how they are mechanistically

Received: December 4, 2024. **Revised:** July 18, 2025. **Editorial Decision:** August 2, 2025. **Accepted:** August 5, 2025

coupled to the core molecular processes they ultimately regulate.

Studies in *S. cerevisiae* identified the nucleosome remodeler ATPases Chd1 and Isw1 as important for maintaining proper nucleosome spacing during transcription elongation [3–6]. While Isw1 is the ATPase subunit of Isw1a and Isw1b complexes, Chd1 is a monomeric nucleosome remodeler [7, 8]. Yeast strains deleted of *CHD1* have reduced nucleosome phasing beyond the first nucleosome of the gene body (+1 nucleosome), increased histone turnover at the 3′ ends of genes, altered distributions of transcription-coupled histone modifications such as H3K4me3 and H3K36me3, and elevated levels of aberrant transcripts arising from inappropriate access to the genome by transcription factors [3, 5, 9–12]. Dual loss of Chd1 and Isw1 in yeast exacerbates the effects of single *chd1*Δ and *isw1*Δ mutations and results in severe changes to nucleosome positions across highly transcribed genes, consistent with significant functional overlap [3, 5, 6]. Moreover, both ATPases are required to resolve tightly packed nucleosomes at the 5′ ends of genes [13]. For Isw1, these effects are mediated through the Isw1b complex, which has a more prominent effect than Isw1a on nucleosome spacing within gene bodies [3, 5, 6, 13]. Chd1 also possesses nucleosome assembly activity that appears to be separable from its remodeling activity and is important for the incorporation of histone variant H3.3 into *Drosophila* chromatin *in vivo* [11, 14–16]. Consistent with its roles in preserving chromatin architecture during transcription elongation, yeast Chd1 is broadly enriched on the bodies of transcriptionally active genes [17–19].

Among the nine CHD family members in metazoans, CHD1 and CHD2 are most similar to *S. cerevisiae* Chd1 [20]. In murine embryonic stem (mES) cells, mCHD2 is enriched at the 5′ ends of highly transcribed genes and shares overlapping peaks with mCHD1 [21]. mCHD2 also occupies chromatin marked with H3K36me3 and is distributed across transcribed genes, a feature that is shared with yeast Chd1 and distinguishes it from mCHD1, which is more enriched at the 5′ ends of genes in mES cells [22, 23]. Importantly, mCHD1 and mCHD2 are critical for cellular differentiation and development. mCHD1 regulates pluripotency and self-renewal of mES cells while mCHD2 is important for neural development [23–26]. *CHD1*$^{-/-}$ and *CHD2*$^{-/-}$ mice die during development [24, 27].

Chd1 employs a twist defect mechanism to induce and then resolve transient DNA bulges in the nucleosome [28–30]. Chd1 contains multiple structured regions (Fig. 1A), including the ChEx region, tandem chromodomains, a two-lobed Snf2-like ATPase domain, a SANT-SLIDE DNA-binding domain (DBD), and a helical C-terminal domain (CHCT) [31–34]. The ChEx region binds the nucleosome acidic patch and competes with other factors that target this exposed surface [34]. The chromodomains distinguish between nucleosomes and free DNA substrates by packing against and inhibiting the ATPase motor [35]. The DBD senses extranucleosomal DNA during remodeling in a sequence-independent manner to centrally position nucleosomes on a chromatin template [36–39]. Newly characterized regulatory elements in human and yeast Chd1 lie between the second ATPase lobe and the DBD. An anchor element positions the remodeler at the entry-side nucleosome acidic patch at an early step in remodeling [40] and an autoinhibitory domain, NegC, competes with flanking activator elements to regulate the transition between the open and closed remodeling states [41]. The CHCT domain of human CHD1 has been characterized through nuclear magnetic resonance (NMR) and has double-stranded DNA (dsDNA) and nucleosome-binding capabilities *in vitro* [33]. However, compared to the other structured domains in Chd1, the CHCT domain is greatly understudied. This domain has been omitted from many biochemical assays, its structure within the context of full-length Chd1 is unresolved, and its functions *in vivo* are unknown [32, 33, 40, 41].

Elucidation of the mechanisms that target Chd1 to actively transcribed genes is important for understanding how nucleosome spacing and histone modification patterns are maintained during transcription elongation. In addition to their roles in substrate selection, the chromodomains of human CHD1 bind to H3K4me3, a modification that marks the 5′ ends of active genes [40, 42–44]. Consistent with this observation, the chromatin occupancy of mouse CHD1 correlates with H3K4me3 and RNA Pol II enrichment at active genes [22, 23]. In contrast, the chromodomains of *S. cerevisiae* Chd1 and human CHD2 are unable to bind to H3K4me3 or do so very weakly [44–47], and *Drosophila* CHD1 does not require chromodomains to interact with actively transcribed chromatin [48]. These observations suggest the possibility of an alternative, conserved mechanism to direct Chd1 to active genes.

In addition to its nucleosome-binding activity, Chd1 interacts with transcription elongation factors and histone chaperones, including Rtf1 and FACT [19, 49, 50]. The ATPase activity of Chd1 is required for the proper distribution of the FACT histone chaperone subunit Spt16 across genes, and Chd1 and FACT coordinately resolve hexasome–nucleosome complexes that arise during transcription elongation [17, 51]. Rtf1 is a subunit of the Polymerase-Associated Factor 1 Complex (Paf1C), a core component of the active RNA Pol II elongation complex [52, 53]. Paf1C directly stimulates transcription elongation and RNA Pol II processivity [53–57], facilitates the deposition of transcription-coupled histone modifications including mono-ubiquitylation of H2B on K123 in yeast (K120 in humans) and H3K4me3 [58–64], and impacts RNA splicing and transcription termination [54, 65, 66]. In metazoans, PAF1C regulates promoter-proximal pausing of RNA Pol II [67, 68]. *S. cerevisiae* Paf1C is composed of five subunits: Paf1, Ctr9, Cdc73, Leo1, and Rtf1; mammalian PAF1C contains a sixth subunit, WDR61/SKI8 [50, 52, 53, 69, 70]. Paf1C interacts with RNA Pol II through direct contacts with RNA Pol II subunits and the elongation factors Spt5 and Spt6 [53, 71–74]. In metazoan systems, RTF1 is more loosely associated with PAF1C [53, 75].

An interaction between Chd1 and Rtf1 is intriguing because Rtf1 travels within Paf1C and with RNA Pol II during transcription elongation, providing an avenue by which Chd1 could access and remodel transcriptionally disrupted nucleosomes. We previously demonstrated at selected genes that Chd1 occupancy is reduced when *RTF1* is deleted or mutated in yeast, and a large region of Chd1, that includes the DBD and CHCT domain, can interact with Rtf1 in a manner requiring the Rtf1 N-terminal region [19, 76]. In *Drosophila*, depletion of Rtf1 reduced Chd1 occupancy on polytene chromosomes, suggesting that an Rtf1-dependent mechanism for targeting Chd1 to active genes could be conserved in other eukaryotes [77]. Here, we demonstrate a direct interaction between a 30 amino acid N-terminal region of yeast Rtf1 and the CHCT domain of yeast Chd1. Mutations that disrupt this interaction result in a buildup of Chd1 occupancy at

the 5′ ends of genes, a 5′ shift of mononucleosomes and other MNase-protected fragments, and altered histone modification patterns. We further demonstrate an interaction between the analogous regions of mouse RTF1 and mCHD1 or mCHD2 and examine the consequences of disrupting these regions in mES cells. This work provides insight into the mechanisms that distribute the nucleosome remodeler Chd1 across active genes and the function of a conserved Chd1 domain that has been largely uncharacterized.

Materials and methods

Yeast strains and media

The *S. cerevisiae* strains used in this study are listed in Supplementary Table S1 and are derived from S288C [78] with the exception of PJ69-4A, which was used in the Y2H assays [79]. Strains were cultured at 30°C in YPD medium supplemented with 400 μM tryptophan or synthetic complete (SC) media lacking indicated amino acids or uracil [80]. *Schizosaccharomyces pombe* strains used for spike-in controls were grown in YES medium (3% glucose, 0.5% yeast extract, with adenine, uracil, histidine, leucine, and lysine at 0.2 g/l) at 30°C (Supplementary Table S1). For selection against *URA3*, SC medium was prepared with 0.1% 5-fluoroorotic acid (5-FOA) (GoldBio, F-230-10). To select for kanamycin or hygromycin resistance, YPD medium supplemented with 400 μM tryptophan and 0.2 g/l Geneticin (Gibco, 11811-023) or 0.3 g/l hygromycin (GoldBio, H-270-1) was used.

Strains containing endogenously expressed *3xHA-rtf1-8-9A*, *3xHA-rtf1-L11A,* and *3xHSV-chd1ΔCHCT* were generated using the *delitto perfetto* approach in which a pCORE cassette that contains a counter-selectable marker is polymerase chain reaction (PCR) amplified from a plasmid with primers specific to both the cassette and the integration locus [81]. To integrate a pCORE cassette at the *RTF1* locus, primers SAT07 and SAT08 containing sequences specific to the pCORE-UH (*Kluyveromyces lactis URA3* and hygromycin resistance) cassette were used. Oligonucleotide sequences are listed in Supplementary Table S2. Stable integration of the pCORE cassettes into a diploid strain generated from crossing KY1691 and KY2822 was confirmed by drug resistance and PCR genotyping. Diploids were then sporulated and haploid strain KY5466 with the pCORE cassette *rtf1Δ::pCORE-UH* was selected for replacement. To integrate a pCORE cassette at *CHD1,* primers containing sequences specific to the pCORE-KU (*K. lactis URA3* and kanamycin resistance) cassette were used. The pCORE cassette was integrated into haploid strain KY3806 to generate *3xHSV-chd1(Δ1353-1468)::pCORE-KU* (KY4361). Stable integration of the pCORE cassette into the strain was confirmed by drug resistance and PCR genotyping. For replacement cassettes, the *RTF1* regions of interest were amplified using primers BTO64 and SAT09 from plasmids KB1653 and KB1654, containing *3xHA-rtf1-8-9A* or *3xHA-rtf1-L11A* in which leucine codons 8 and 9 or 11 were substituted with alanine codons. The *chd1ΔCHCT* truncation was PCR amplified from the *CHD1* locus using SAT79 and SAT81, a primer that encoded a stop codon after amino acid 1352. Amplified fragments were transformed into the appropriate pCORE-containing strain (see above) and recombinants were selected on 5-FOA medium, followed by screening for sensitivity to hygromycin or G418, to generate KY3843, KY3844, and KY4363. Strains were verified by PCR genotyping. Genotypes were further confirmed by inspection of the targeted locus in genomics data. The *GAL1p-FLO8-HIS3* reporter was introduced into strains using genetic crosses as previously described [80].

An HSV (herpes simplex virus) epitope-tagged spike-in control strain was generated from *S. pombe* strain FWP568 (gift of Fred Winston). A hygromycin resistance cassette (purchased as a plasmid from Addgene *pFA6a-6xGLY-HSV-hphMX4*) [82] was amplified using primers SAT17 and SAT18. Extended homology arms were generated upstream (using primers SAT41 and SAT42) and downstream (using primers SAT43 and SAT44) of the *S. pombe hrp1* locus, which encodes a CHD family protein [83]. The homology arms and cassette were assembled using PCR, and the PCR product was used to generate KP08 by integrative transformation of FWP568 [84].

mES cell culture

ES-E14TG2a (E14) embryonic stem (ES) cells from male *Mus musculus* origin (RRID:CVCL9108) were cultured in Dulbecco's modified Eagle medium (Sigma–Aldrich, D6546-500 ml), 10% fetal bovine serum (Sigma–Aldrich, F2442), nonessential amino acids (Corning, 25-025-CI), 2 mM L-glutamine (Corning, 25-005-CI), β-mercaptoethanol, and Leukemia Inhibitory Factor (LIF). Unless otherwise noted, cells were cultured under naïve conditions (serum/LIF + 2i), with 3 nM CHIR99021 GSK inhibitor (Med Chem Express, HY-10182/CS-0181) and 1 nM PD0325901 MEK inhibitor (Med Chem Express, HY-10254CS-0062). Cells were passaged every 48 h using 0.02% trypsin (Corning, 25-052-CI) and quenching with fresh medium. ES cells were grown on plates precoated with 0.2% porcine skin gelatin type A (Sigma–Aldrich, G1890) at 37°C in a humidified incubator with 5% CO_2. Routine anti-mycoplasma cleaning was conducted within tissue culture hoods (LookOut DNA Erase spray) and cell lines were screened to confirm no mycoplasma presence.

CRISPR/Cas9 targeting

mES cell lines were generated with CRISPR/Cas9 technology using single guide RNAs (sgRNAs) and homology constructs that were transfected into low passage wild-type mES cells to produce three cell lines: *chd1ΔCHCT* (two clones), *chd2ΔCHCT* (three clones), and *rtf1(AAAA)* (three clones). sgRNAs were designed using the CRISPick algorithm [85, 86]. sgRNA sequences were purchased as primers and cloned into the px330-U6-Chimeric-BB-CBh-hSpCas9 plasmid containing a PGK-puromycin resistance cassette inserted between NotI and NarI restriction sites (see Supplementary Table S3) [87, 88]. For *chd1ΔCHCT* and *chd2ΔCHCT* targeting, two sgRNAs each were used to generate two cut sites while one sgRNA was used for *rtf1(AAAA)* targeting. Homology constructs were purchased from Thermo Fisher Scientific as GeneArt (see Supplementary Table S4 for recombinant homology sequences). Purchased homology constructs were cloned into TOPO vectors using the standard cloning protocol (see Supplementary Table S5 for plasmids used in CRISPR/Cas9 targeting). To generate *chd1ΔCHCT*, *chd2ΔCHCT,* and *rtf1(AAAA)* cell lines, 3 μg of each plasmid was transfected into wild-type mES cells using FuGENE HD (Promega, E2311). Forty-eight hours post-transfection, the medium was

replaced with medium containing 2 μg/ml puromycin to select for transfected cells. Seventy-two hours post-transfection, the medium was replaced with fresh antibiotic-free ES cell medium. Individual clones were manually selected 8 days post-transfection. Clones were screened through genomic DNA extraction and PCR genotyping. For *chd1*Δ*CHCT* and *chd2*Δ*CHCT*, PCR was performed using multiplexed primers to screen for an appropriate PCR product size (see Supplementary Table S3). The *rtf1*(*AAAA*) cell lines were verified by PCR genotyping followed by restriction enzyme digestion with SacI, as the altered DNA sequence (LLSL amino acids 73–76 to AAAA) results in a novel SacI site. Homozygotes for all cell lines were verified by sequencing the PCR products and western blotting to confirm protein expression and relevant protein size shift. Genotypes were further confirmed by inspection of the targeted locus in genomics data. Experiments were performed with two independently generated clones in technical duplicate for *chd1*Δ*CHCT* and three independently generated clones with a single technical replicate for *chd2*Δ*CHCT*, *rtf1*(*AAAA*), and wild type.

Endoribonuclease-digested short interfering RNA generation

Endoribonuclease-digested short interfering RNAs (esiRNAs) were generated as previously described [89]. Sequences for esiRNAs are described in Supplementary Table S3. Briefly, oligonucleotides to the region of interest with the T7 promoter were used to amplify the target location. A second PCR was performed to further amplify these sequences. This PCR product was used as template for an *in vitro* transcription (IVT) reaction using T7 RNA Polymerase. IVT products were digested with Shortcut RNase III (NEB, M0245S) and purified using the PureLink RNA Mini Kit (Invitrogen, 12183018A). Purified esiRNAs were visualized on a 1.5% agarose gel to confirm appropriate digestion.

esiRNA transfection

Transfections were performed using 3500 ng of either control (GFP, nontargeting), *CHD1*, or *CHD2* esiRNAs, 30 μl of Lipofectamine 3000 (Invitrogen, L3000150), and OptiMEM (Gibco, 31985070). Reactions were incubated for 15 min at room temperature, added to 1400 000 cells in suspension, and transferred to a pre-gelatinized 10 cm plate. Cells were incubated overnight at 37°C in a humidified incubator with 5% CO_2. After 16 h, the transfection medium was replaced with 8 ml fresh ES cell medium, as described above. Forty-eight hours post transfection, cells were harvested to confirm depletion efficiency and, in parallel, cells were flash frozen for CUT&RUN experiments.

Plasmid construction

To generate plasmids that encode full-length 3xHA-Rtf1 with amino acid substitutions to alanine, plasmid pLS21-5 [90], expressing wild-type 3xHA-Rtf1, was digested with EcoRI and BglII or NdeI and BglII (see Supplementary Table S6 for plasmids related to yeast experiments). Primers with substituted sequences (see Supplementary Table S2) were used to amplify from pLS21-5 for insertion of fragments into pLS21-5 by Gibson assembly (NEB, E5510S) or for site-directed mutagenesis [91]. The plasmid pARL01, a derivative of pGBT9 [92] encoding GBD-Rtf1(1–30), was used as the template to generate plasmids encoding alanine substitutions in the Rtf1 N-terminal region. pARL01 was restriction digested and primers with mutated sequences were used to amplify from pARL01. Plasmids were prepared by Gibson assembly. pGAD-Chd1(863–1468) is from [19]. To create pGAD-Chd1(1353–1468), the CHCT region was amplified by PCR from a plasmid containing *CHD1* sequence, using PSO551 and HMO2, and ligated via Gibson assembly into the BamHI and SalI sites in a digested pGAD424 vector backbone [92].

To generate Y2H plasmids with sequences for mouse RTF1, CHD1, and CHD2, DNA fragments encoding CHD1 amino acids 1321–1506, CHD2 amino acids 1331–1561, or RTF1 amino acids 1–321 were codon-optimized for expression in yeast and purchased from Invitrogen (GeneArt; see Supplementary Table S4). Gibson assembly was used to subclone desired fragments into pGBT9 or pGAD424 [92], the GBD-EV or GAD-EV plasmid vectors, respectively, to generate GBD-mRTF1(1–115), GBD-mRTF1(1–321), GBD-mRTF1(66–321), GAD-mCHD1(1321–1506), and GAD-mCHD2(1331–1561). For constructs GAD-mCHD1(1378–1512) and GAD-mCHD2(1432–1567), primers with yeast codon-optimized sequences were used to generate CHD1 and CHD2 fragments by PCR from the GAD-mCHD1(1321–1506) and GAD-mCHD2(1331–1561) plasmids. Plasmid GBD-mRTF11(66–95) was constructed with primers SAT64 and SAT65 that encompass the 66–95 sequence. To construct plasmids encoding alanine-substituted RTF1 sequences, plasmids GBD-RTF1(1–115) and GBD-RTF1(1–321) were used as templates for PCR with primers containing the desired mutations, and the amplified fragments were cloned into linearized pGBT9. See Supplementary Table S2 for the list of primers used to generate codon-optimized Y2H plasmids. All plasmids were verified by DNA sequencing.

Serial dilution growth assays

Yeast cultures were grown to saturation at 30°C in 5 ml of appropriate media overnight. The optical density (OD) of each culture was measured, and 1 OD unit of cells was diluted in sterile water. Five-fold serial dilutions were prepared and transferred from a sterile 96-well plate to agar media using an 8 × 6 array pinner (Sigma–Aldrich, R2383). Plates were incubated at 30°C and imaged daily for at least 3 days.

Y2H experiments

Strain PJ69-4A was co-transformed with *TRP1*-marked GBD and *LEU2*-marked GAD plasmids [79]. Cultures of transformed cells were grown overnight at 30°C in SC-Leu-Trp medium, serially diluted by five-fold, and then plated onto SC-Leu-Trp, SC-Leu-Trp-His, SC-Leu-Trp-His + 2 mM 3-aminotriazole (3-AT), or SC-Leu-Trp-His + 5 mM 3-AT (Sigma, 18056-25G). Plates were incubated at 30°C and imaged daily for at least 3 days.

Multiple sequence alignments

Protein sequences were retrieved from UniProt, aligned with Clustal Omega using default parameters, and visualized in Jalview [93–95]. The following sequences of Rtf1 homologs were used: P53064 (*S. cerevisiae*), A2AQ19 (*M. musculus*), and Q92541 (*Homo sapiens*). The following sequences of Chd1 homologs were used: P32657 (*S. cerevisiae*), O14139 (*S. pombe*), F4IV99 (*Arabidopsis thaliana*), O17909 (*Caenorhabditis elegans*), Q7KU24 (*Drosophila melanogaster*), B6ZLK2 (*Gallus gallus*), F7D0V6 (*Xenopus*

tropicalis), P40201 and E9PZM4 (*M. musculus* CHD1 and CHD2, respectively).

In vivo site-specific photo-crosslinking

BPA (p-benzoyl-L-phenylalanine) crosslinking experiments were performed as described [63, 96] except the extracts were made using a urea-based lysis buffer (8 M urea, 300 mM NaCl, 50 mM Tris–HCl, pH 8.0, 0.1% NP40, 10 mM imidazole, 1 mM phenylmethylsulfonyl fluoride [PMSF]). Yeast strains KY2937 or KY5011 were co-transformed with pLH158/LEU2, a transfer RNA/transfer RNA synthetase-expressing plasmid to promote BPA incorporation, and either a plasmid overexpressing wild-type Rtf1 protein (KB851) or a plasmid with an amber codon replacing codon 4 of *RTF1* (KB1424). Yeast cells were grown to late log phase in SC medium lacking leucine and tryptophan and containing 1 mM BPA (BACHEM, F-2800). Twenty OD units of cells were harvested, and crosslinking was performed in 1 ml of ddH_2O for 10 min with 365 nm UV light. Urea-based lysis buffer (200 µl) was added to the cell pellet and extracts were made by vortexing with glass beads. Lysates were cleared by centrifugation for 15 min in a microcentrifuge and sodium dodecyl sulfate–polyacrylamide gel electrophoresis (SDS–PAGE) loading buffer was added to 1X. Samples were separated on 4%–15% SDS–polyacrylamide gels (Bio-Rad Mini-PROTEAN TGX Stain-Free, 4568086), where the 75 kD molecular weight marker was run to the bottom of the gel. To visualize total protein levels, gels were imaged per manufacturer's instructions prior to transfer for western blot analysis. Western blot analysis was performed using α-Rtf1 antisera [52] (1:2500) or α-HSV antibody (Sigma–Aldrich, H6030; 1:2000) to detect Chd1 proteins.

Protein structure prediction

Using standard parameters, AlphaFold 3 was used to predict the structures of Rtf1 N-terminal regions with Chd1 CHCT domains [97]. Predictions were performed three times with different seeds. Average interface predicted template modeling (ipTM) scores (with standard deviation) were: 0.71 ± 0.01 for yRtf1(1-30)–yChd1(1353–1468) and 0.50 ± 0.02 for mRTF1(1–115)–mCHD1(1378–1512). Top scoring models are displayed in the figures. The pLDDT scores and predicted alignment error (PAE) plots are provided as a measure of confidence in the models. Structures were visualized in ChimeraX [98]. Calculations of RMSD between the AlphaFold models and the human CHCT NMR structure (PDB: 2N39) [33] were performed in ChimeraX. RMSD values are given in the figure legends.

Cryptic transcription initiation analysis

Cryptic transcription initiation at the *GAL1p-FLO8-HIS3* reporter was measured as described [9]. For experiments involving an *rtf1*Δ strain (KY1370) transformed with *TRP1*-marked *CEN/ARS* plasmids, cells were grown in SC-Trp liquid medium, serially diluted, and spotted onto SC-Trp and SC-His-Trp + gal (galactose, 2%) solid media. For experiments using strains containing integrated *rtf1* or *chd1* mutations, cells were grown in SC complete medium, serially diluted, and spotted onto SC complete and SC-His + gal solid media. Plates were incubated at 30°C and images were taken on the days indicated in the figures.

ChIP-quantitative PCR

Saccharomyces cerevisiae chromatin was prepared as described previously [71]. For immunoprecipitation, 700 µl chromatin in 1× FA buffer containing 0.1% SDS, 1 mM PMSF, and 275 mM NaCl was incubated with antibody against hemagglutinin (HA) [40 µl; Santa Cruz HA-probe Antibody (F-7) AC, sc-7392] or HSV (2.5 µl; Sigma–Aldrich, H6030) and incubated overnight at 4°C with end-over-end rotation. Separately, 50 µl chromatin input sample in 1× FA buffer containing 0.1% SDS, 1 mM PMSF, and 275 mM NaCl received no antibody and was incubated overnight at 4°C. The next day, for HSV IPs, 30 µl 50% slurry of Protein A Sepharose beads (Cytiva, 17-5280-01) were washed twice with 1× FA buffer containing 0.1% SDS, 275 mM NaCl, and 1 mM PMSF and added to immunoprecipitation (IP) reactions. HSV IPs with Protein A beads were incubated for 1 h at 4°C with end-over-end rotation. For IP washes, beads were pelleted at 3000 rpm for 10 s and washed for 4 min each in 500 µl of the following buffers: (i) 1× FA buffer containing 0.1% SDS, 275 mM NaCl, and 1 mM PMSF, (ii) 1× FA buffer containing 0.1% SDS, 500 mM NaCl, and 1 mM PMSF, (iii) TLNNE containing 1 mM PMSF [TLNNE: 10 mM Tris–HCl, pH 8.0, 250 mM LiCl, 1 mM ethylenediaminetetraacetic acid (EDTA), 0.5% NP-40, 0.5% sodium deoxycholate], and (iv) Tris-EDTA (TE) buffer (1 mM EDTA, 10 mM Tris–HCl, pH 8). IPs were eluted from beads in 50 mM Tris–HCl, pH 8, 10 mM EDTA, and 1% SDS at 65°C for 10 min and washed again in TE. Immunoprecipitated and input DNA were treated with Pronase (800 µg/ml) for 1 h at 42°C and crosslinks were reversed overnight at 65°C. Immunoprecipitated DNA was then purified using the QIAquick PCR purification kit (Qiagen, 28106) according to manufacturer's instructions. Final volumes were 100 µl 0.5× TE for IPs and 900 µl 0.5× TE for inputs.

PCR reactions were made in 20 µl volume with 5 µl IP or input DNA, 10 µl SYBR (2× qPCRBIO SyGreen Blue Mix Hi-ROX, 17-505B), 1.2 µl 5 µM primer mix, and water. Reactions were split into 10 µl volumes for technical duplicates. Each sample was tested in biological triplicate and technical duplicate. PCR conditions were: 10 s initial denature, and 35 cycles of 5 s 95°C denature and 30 s 60°C elongation. Primer efficiencies were calculated for each primer pair by performing 10-fold serial dilutions of genomic DNA and performing quantitative PCR (qPCR) in technical triplicate. A line of best fit through the Cq values of the dilution series was obtained and used to calculate primer efficiency. The chromatin immunoprecipitation (ChIP)-quantitative PCR (ChIP-qPCR) primers and their efficiencies are found in Supplementary Table S2. Relative chromatin occupancy was calculated as described in [99].

ChIP-sequencing

Yeast chromatin was prepared as described previously [71]. *Schizosaccharomyces pombe* chromatin from strain KP08 was spiked-in to *S. cerevisiae* chromatin at a 1:9 protein ratio upon thawing of sheared chromatin. Chromatin was quantified using the Pierce BCA kit (Thermo Fisher Scientific, 23225). IPs were performed with 500 µg (for histone IPs) or 1000 µg (for all other IPs) spiked-in chromatin and samples were diluted to 700 µl or 1.4 ml in 1× FA buffer containing 0.1% SDS and 1 mM PMSF, respectively. ChIPs were performed with antibodies against the following epitopes/proteins: HSV

(Sigma–Aldrich, H6030; 5 µl per 1000 µg), HA (Santa Cruz, HA-probe Antibody (F-7) AC, sc-7392; 60 µl per 1000 µg), Rpb1 (8WG16; BioLegend, 664906; 4 µl per 1000 µg), H3 (Abcam, ab1791; 1 µl per 500 µg), H3K4me3 (Active Motif 39159, 39160; 2.5 µl per 500 µg), and H3K36me3 (Abcam ab9050: 6 µg per 500 µg). After overnight incubation of primary antibodies with chromatin, Protein A Sepharose beads (Cytiva, 17-5280-01) were added to HSV, 8WG16, and H3K4me3 reactions in an amount of 30 µl beads (50% slurry) per 500 µg chromatin. Protein G Sepharose beads (Cytiva, 17-0618-01) were added to H3 and H3K36me3 in an amount of 30 µl beads (50% slurry) per 500 µg chromatin. Samples with Protein A or G beads were rotated end-over-end for 2 h at 4°C. IP reactions were performed as described above for ChIP-qPCR, with input samples processed in parallel. DNA was eluted in 100 µl 0.5× TE. Libraries were prepared with the NEB Next II Ultra DNA library kit (NEB, E7645L) using 500 pg DNA input. Library quality was verified using fragment analysis (Fragment Analyzer, Advanced Analytical) and submitted for sequencing on an Illumina NextSeq 500 or 2000 instrument for paired-end sequencing to a depth of ∼10 million uniquely mapped reads per sample.

Indirect immunofluorescence

Yeast cultures were grown to mid-log phase overnight at 30°C in YPD medium supplemented with tryptophan. Cells (5 ml) were centrifuged for 3 min at 3000 rpm and then resuspended in fresh growth medium with 4% formaldehyde, followed by incubation with shaking for 10 min at 30°C. Cells were spun as before and then resuspended in KM solution (40 mM potassium phosphate, pH 6.5, 500 µM magnesium chloride) with 4% formaldehyde and then shaken for 1 h at 30°C. Cells were then spun at 2000 rpm and washed twice in KM solution and once in KMS (40 mM potassium phosphate, pH 6.5, 500 µM magnesium chloride, 1.2 M sorbitol). Cells were resuspended in 0.5 ml KMS solution and then treated with 30 µl Zymolyase 100T (US Biological, Z1004250MG) 10 mg/ml stock solution for 25 min at 37°C, followed by centrifugation at 2000 rpm for 2 min. Spheroplasts were washed with KMS solution and then resuspended in 200 µl and placed on ice. Slides were prepared with 1x poly-L-lysine (Sigma–Aldrich, P1399) and incubated for 10 min in a humidified chamber, then washed five times with water. Twenty µl cells were added to slides and incubated at room temperature for 10 min. Slides were plunged into cold methanol, incubated at −20°C for 6 min, and subsequently plunged into cold acetone for 30 s. Acetone was evaporated near a heat block at 100°C. Blocking solution [phosphate-buffered saline (PBS) with 0.5% bovine serum albumin (BSA) and 0.5% ovalbumin] was applied to the slides for 1 h at 37°C. After removing the blocking solution with aspiration, a 1:250 dilution of primary antibody (anti-HSV; Sigma–Aldrich, H6030) in PBS (30 µl volume) was placed on the slides overnight at 4°C in a humidified chamber. After removing the primary antibody with aspiration, the cells were washed with blocking solution and incubated with blocking solution for 5 min three times. Alexa Fluor 568 secondary antibody (Invitrogen A-11011; 25 µl) was added to the slides, which were then stored in a dark chamber for 2 h at 30°C. Slides were washed thrice with blocking solution for 5 min at room temperature. Mounting solution with 4′,6-diamidino-2-phenylindole (DAPI) stain (Invitrogen, P36966) was applied to the slides and then coverslips were added. Cells were imaged with a confocal microscope (Nikon Confocal, A1R).

Micrococcal nuclease sequencing

The micrococcal nuclease sequencing (MNase-seq) protocol was adapted from [100]. Yeast cultures were grown to log phase (OD = 0.5–0.6), and cells were crosslinked with 2% formaldehyde, quenched with glycine, pelleted, and flash frozen as described [100]. Cell pellets were resuspended in 19 ml sorbitol-Tris buffer (1 M sorbitol, 50 mM Tris–HCl, pH 7.4, 125 mM ß-mercaptoethanol) and then spheroplasted by adding 5 mg Zymolyase 100T (US Biological, Z1004250MG) dissolved in 1 ml sorbitol-Tris buffer for 30 min at 30°C while rotating. Spheroplasting efficiency was visually determined under the microscope after mixing 10 µl spheroplasts with 10 µl 10% SDS. Spheroplasts were centrifuged at 4000 rpm for 10 min at 4°C. The supernatant was removed, and the pellet was resuspended to 5 ml in NP buffer (1 M sorbitol, 50 mM NaCl, 10 mM Tris–HCl, pH 7.4, 5 mM $MgCl_2$, 1 mM $CaCl_2$, 0.075% NP40, 1 mM ß-mercaptoethanol, and 500 µM spermidine). MNase (500 units; Sigma, N5386) was resuspended from lyophilized powder in 500 µl Ex50 buffer [10 mM HEPES, pH 7.5, 50 mM NaCl, 1.5 mM $MgCl_2$, 0.5 mM ethylene glycol-bis(β-aminoethyl ether)-N,N,N',N'-tetraacetic acid (EGTA), pH 8.0, 10% glycerol (v/v), 1 mM DTT, and 0.2 mM PMSF] and stored in aliquots at −20°C. Spheroplasts in 600 µl aliquots were treated with MNase in a titration ranging from 2 to 4.5 µl MNase for 20 min at 37°C with rotation. The reaction was quenched, and samples were treated with proteinase K followed by reversal of crosslinks at 65°C as described [100]. DNA was purified by phenol extraction, followed by isopropanol precipitation. The DNA pellet was resuspended in 40 µl 10 mM Tris–HCl, pH 7.5. Resuspended DNA was treated with 5 µl RNase A (Thermo Fisher Scientific, EN0531) for 1 h at 37°C.

To verify MNase digestion, 15 µl of DNA was purified using the E.Z.N.A. Cycle Pure Kit (Omega Bio-Tek, D6492) and separated on a 2% agarose-TBE gel. The 3.5 µl MNase-treated condition was chosen for all samples based on the titration series, and digested chromatin samples were processed without DNA size selection. *Schizosaccharomyces pombe* MNase-treated chromatin was separately prepared and mononucleosome-sized DNA fragments were gel extracted and spiked-in to *S. cerevisiae* MNase-digested DNA. Spiked-in MNase-treated DNA was purified using the E.Z.N.A. Cycle Pure kit. Sequencing libraries were prepared with the NEB Next II Ultra DNA library kit (NEB, E7645L) using 50 ng DNA input and three PCR cycles. Library quality was verified using fragment analysis (Fragment Analyzer, Advanced Analytical) and submitted for sequencing on an Illumina NextSeq 500 or 2000 instrument for paired-end sequencing to a depth of ∼15 million uniquely mapped reads per sample.

Western blotting

Yeast protein extracts were prepared either by trichloroacetic acid (TCA; for GBD, GAD, and associated G6PDH western blots) [63] or NaOH [101] protein extraction methods (remaining western blots). Proteins were resolved on either 8% or 15% SDS–polyacrylamide gels. Proteins were transferred to nitrocellulose (Bio-Rad, 1620094), with the exception of GBD, GAD, G6PDH, and H3K36me3, which were

transferred to polyvinylidene difluoride (PVDF) membranes (Immobilon, PVH00010). Membranes were blocked for 1 h in 5% milk + Tris-buffered Saline Tween-20 (TBST) and subsequently incubated with primary antibodies/antisera against HSV (1:2000), HA (1:5000), Rpb1 (8WG16; 1:500), H3 (1:15 000), H3K4me3 (1:2000), H3K36me3 (1:1000, 3% BSA in Phosphate Buffered Saline with Tween 20 [PBST]), or Sse1 (1:1000) for 2 h at room temperature in 5% milk + TBST (unless otherwise indicated). Membranes probed with primary antibodies GBD (1:1000), GAD (1:1000), and G6PDH (1:20 000) were incubated overnight at 4°C in 5% milk + TBST.

Western blot analysis of GBD-mRTF1 constructs was performed as follows. Experiments analyzing the expression of yeast Rtf1 fusions to the Gal4 DNA-binding domain (GBD) by western blotting used SC-577 (Santa Cruz). However, this antibody is no longer available, and the tested replacement antibodies reacted non-specifically with proteins that obscured detection of the GBD-mRTF1 proteins on western blots. To circumvent this complication, we performed immunoprecipitations with SC-510-AC (Santa Cruz) on whole cell extracts prepared from strains expressing GBD-mRTF1 and performed western analysis using a different GBD antibody (Sigma–Aldrich, G3042), with the expectation that the cross-reacting background bands of the two antibodies would be different. Cells were grown to $OD_{600} = 0.5–0.6$. Extracts were prepared by bead-beating and quantified by Bradford analysis using bovine serum albumin standards. Immunoprecipitations were performed with 500 μg of extracts containing 20 mM HEPES–KOH, pH 7.4, 125 mM potassium acetate, 20% glycerol, 1 mM EDTA, pH 8.0, 1 mM DTT, and 1 mM PMSF. Extracts were incubated at 4°C overnight with 15 μl bead volume of SC-510-AC that had been equilibrated with the same buffer. Beads were washed three times with the same buffer and eluted by boiling in SDS–PAGE loading buffer. Approximately one-third of the immunoprecipitation was separated on a 15% SDS–polyacrylamide gel and transferred to a nitrocellulose membrane. Western analysis was performed using the G3042 primary antibody (Sigma–Aldrich) in 5% dry milk in TBST with an overnight incubation at 4°C. To reduce the detection of the heavy and light chain from the immunoprecipitating antibodies, a 1:1000 dilution of Rabbit True Blot (Rockland, 18-8816-13) was used as the secondary antibody. Bands were visualized using chemiluminescence (Thermo Fisher Scientific, 34580) on a Bio-Rad Chemidoc XRS system.

Mouse protein extracts were prepared by RIPA [88] or acid-based histone extraction. For acid-based histone extraction, cells were lysed in 200 μl Triton Extraction Buffer (TEB; 0.5% Triton X-100, 2 mM PMSF, 0.02% sodium azide diluted in 1X Dulbecco's PBS) for 10 min. Lysate was centrifuged for 10 min at 650 g at 4°C and supernatant was discarded. Cells were washed in 100 μl TEB and centrifuged as before and supernatant was removed. Lysate was resuspended in 50 μl 0.2N HCl and rotated overnight at 4°C. Extracts were then centrifuged for 15 min at 4°C and the supernatant was retained, flash frozen, and stored at −75°C. Protein concentrations were determined using the Pierce BCA kit. Extracts were diluted in SDS loading buffer and loaded at either 50 μg protein (CHD1, CHD2, RTF1) or 10 μg protein (H3, H3K4me3, H3K36me3, Actin) onto 8% or 15% SDS–polyacrylamide gels and run at 150 V. Proteins were transferred to nitrocellulose membranes. For RTF1 (Invitrogen, PA5-52330), CHD1 (Diagenode, C15410334), and CHD2 (Invitrogen, MA5-47275) blots, loading control was measured with REVERT 700 total protein stain (LICORbio, 926-11011) and imaged by LI-COR (LI-COR Odyssey DLx Imager). Membranes were blocked for 1 h in 5% milk + PBST. For RTF1 (1:500, 5% milk in PBST), CHD1 (1:2000, 5% BSA in PBST), and CHD2 (1:500 in PBST) blots, membranes were incubated with primary antibody overnight at 4°C. For H3 (1:1000 in PBST), H3K4me3 (1:2500, 5% milk in PBST), H3K36me3 (1:1000, 5% milk in PBST), and actin (1:5000 in PBST) blots, membranes were incubated with primary antibody for 2 h at room temperature. Following incubation with secondary antibodies (1:5000) for 1 h at room temperature, membranes were imaged with Pico Plus chemiluminescence substrate (Super Signal West Pico PLUS Chemiluminescent Substrate, Thermo Fisher Scientific, 34580) on the ChemiDoc XRS imaging platform (Bio-Rad).

CUT&RUN

CUT&RUN was performed as described using 100 000 nuclei per reaction [88, 102–105]. Three replicates for wild-type and mutant lines were assayed, except for *chd1ΔCHCT* where two technical replicates of two cell lines were used. For esiRNA depletion experiments, three replicates were performed for control (*GFP* KD), *CHD1* KD, and *CHD2* KD. Nuclei were extracted using a nuclear extraction buffer (20 mM HEPES–KOH, pH 7.9, 10 mM KCl, 0.5 mM spermidine, 0.1% Triton X-100, 20% glycerol, protease inhibitors) and flash frozen. Nuclei were thawed, and nuclei extracted from *Drosophila* S2 cells were added at 1:99 dilution for spike-in normalization. Nuclei were bound to concanavalin A beads (25 μl bead slurry per 100 000 nuclei, Polysciences, 86057-10), blocked with blocking buffer (20 mM HEPES–KOH, pH 7.5, 150 mM NaCl, 0.5 mM spermidine, 0.1% BSA, 2 mM EDTA, protease inhibitors), and washed using a wash buffer (20 mM HEPES–KOH, pH 7.5, 150 mM NaCl, 0.5 mM spermidine, 0.1% BSA, protease inhibitors). Nuclei were incubated overnight at 4°C with rotation in wash buffer with rabbit anti-Chd1 (Diagenode 15410334, 1:50). Nuclei were incubated for 1 h at room temperature with rotation with rabbit anti-H3K4me3 (Sigma–Aldrich 05-745R, 1:100) or anti-H3K36me3 (Invitrogen MA5-24687, 1:100). Samples were washed twice with wash buffer and incubated for 30 min at room temperature with rotation in wash buffer containing recombinant Protein A-MNase (1:250). Samples were washed twice with wash buffer and equilibrated at 0°C in an ice bath. Three millimolar $CaCl_2$ was added to each sample to activate MNase cleavage and digestions were performed in an ice bath for 30 min. Digestion for H3K4me3 samples was stopped after 30 min using a stop buffer (20 mM EDTA, 4 mM EGTA, 200 mM NaCl, 50 μg/ml RNase A). Samples were incubated at 37°C for 20 min to release genomic fragments and fragments were then separated through centrifugation. Digestion for Chd1 samples was stopped after 30 min using a low salt stop treatment (10 mM EDTA, 2 mM EGTA, 150 mM NaCl, 5 mM Triton-X). Samples were incubated at 4°C for 1 h to release genomic fragments. The salt concentration was increased to 500 mM for Chd1 samples, RNase A was added, and samples were incubated at 37°C for 20 min to release genomic fragments. Libraries were built using NEB Next II Ultra DNA library kit (NEB E7645L) and AMPure XP beads (Beckman Coulter A63881) purifications. Fragments were PCR ampli-

fied with 15 cycles. Samples were then pooled and paired-end sequenced on an Illumina NextSeq2000 to a depth of ∼10 million uniquely mapped reads per sample.

ATAC-sequencing

ATAC-sequencing (ATAC-seq) was performed as described [88, 106]. Nuclei were extracted from 120 000 cells in Lysis buffer (10 mM Tris–HCl, pH 7.5, 10 mM NaCl, 3 mM $MgCl_2$, 0.1% NP-40, 0.1% Tween-20, 0.01% digitonin) Extracted nuclei were flash frozen in liquid nitrogen and stored at −75°C. Nuclei were resuspended in 50 µl Transposase mix (25 µl 2× Tagmentation Buffer, 16.5 µl 1× PBS, 0.5 µl 10% Tween-20, 0.5 µl 1% digitonin, 2.5 µl Tagmentase, 5 µl nuclease-free water) and incubated at 37°C for 30 min in a thermomixer shaking at 1000 rpm. DNA was purified and PCR amplified for nine cycles. Libraries were run on a 1.5% agarose gel and fragments sized 150–700 bp were then gel-extracted. Libraries were paired-end sequenced on an Illumina NextSeq2000 to a depth of ∼50 million uniquely mapped reads per sample.

ChIP-sequencing analysis

Integrity of sequencing data was verified by fastqc version 0.11.9. Fastq files were trimmed with trimmomatic version 0.38 with parameters ILLUMINACLIP:TruSeq3-PE.fa:2:30:10 LEADING:3 TRAILING:3 SLIDINGWINDOW:4:15 CROP:36 MINLEN:24 [107]. Reads were aligned to a combined genome containing *S. cerevisiae* and *S. pombe* using bowtie2 version 2.4.1 with parameters -q -N 1 -X 1000 for paired-end sequencing. *Saccharomyces cerevisiae* and *S. pombe* reads were then separated into different bam files for each genome [108]. Reads were counted with SAMtools version 1.12 flagstat [109]. Normalized bigwigs were generated using deepTools version 3.3.0 bamcoverage with parameters –extendReads –binSize 10 –scaleFactor x, where the scaling factor was determined for each sample using *S. pombe* reads as described [110, 111]. Normalized bigwigs for 2–5 biological replicates were averaged using WiggleTools and the 'mean' function [112]. Pearson correlation values for replicate samples are provided in the Supplementary data file.

Factor occupancy was evaluated using a bed file spanning the +1 nucleosome dyad to transcription termination site (TTS) with data obtained from [113]. Genes that were a minimum of 1 kb in length from the +1 nucleosome dyad to the TTS were analyzed, and we focused on the top quintile of genes with maximum HSV-Chd1 occupancy in our wild-type ChIP-sequencing (ChIP-seq) data set ($n = 784$ genes). In another size class, we focused on genes that were a maximum of 1 kb from the +1 nucleosome dyad to the TTS and examined the first 500 bp of these genes according to maximum wild-type HSV-Chd1 ChIP-seq occupancy ($n = 324$ genes). To determine regions with maximum factor occupancy for HSV-Chd1 (or for RNA Pol II, as in Fig. 2B), the deepTools plotHeatmap function with –sortRegions 'descend' and –sortUsing 'max' were used to generate sorted bed files [111]. Bed files for HSV-Chd1 data were then subset to identify the top quintile of genes and plotted with deepTools computeMatrix and plotHeatmap. To generate metaplots, the output of deepTools plotProfile containing binned data (10 bp) from 200 bp upstream of the +1 nucleosome and 1 kb beyond for each factor and respective genotype was loaded into RStudio version 2022.7.1.554. The maximum data point for each genotype was determined and plotted as a vertical line in GraphPad Prism 10. To generate violin plots, the matrix file from deepTools plotHeatmap containing binned data (10 bp) from 200 bp upstream of the +1 nucleosome and 1 kb beyond was obtained for each factor and respective genotype and was loaded into RStudio version 2022.7.1.554. The bin of maximum enrichment for each factor in each strain was identified for every gene individually. The bins of maximum occupancy for each gene were then plotted (as violin plots) with the median represented with the black dotted line and the interquartile range also represented. Violin plots with these data were generated in GraphPad Prism 10, where the vertical lines denote median (black line) and interquartile ranges of the data (colored lines).

MNase-seq analysis

Integrity of sequencing data was verified by fastqc version 0.11.9. Fastq files were trimmed with trimmomatic version 0.38 with parameters ILLUMINACLIP:TruSeq3-PE.fa:2:30:10 LEADING:3 TRAILING:3 SLIDINGWINDOW:4:15 CROP:36 MINLEN:24 [107]. Reads were aligned to a combined genome containing *S. cerevisiae* and *S. pombe* using bowtie2 version 2.4.1 with parameters -q -N 1 -X 1000 for paired-end sequencing [108]. *Saccharomyces cerevisiae* and *S. pombe* reads were then separated into different bam files for each respective genome. Reads were counted with SAMtools version 1.12 flagstat [109]. Due to variability introduced when using *S. pombe* spike-in normalized bigwigs, CPM (Counts Per Million) analysis normalization was used. Normalized bigwigs were generated using deepTools version 3.3.0 bamcoverage with parameters –normalizeUsing CPM –MNase –binSize 1 –smoothLength 10 –minFragmentLength 137 –maxFragmentLength 157 to examine mononucleosome-sized fragments [111]. Other MNase-protected fragments were bioinformatically size-selected using bamCoverage, including subnucleosomes (90–110 bp), hexasome–nucleosome complexes (230–270 bp), and dinucleosomes (290–350 bp). Normalized bigwigs for two to five biological replicates were averaged using WiggleTools and the 'mean' function [112]. Information on replicates is provided in the Supplementary data file. We generated heatmaps with deepTools computeMatrix and plotHeatmap [111]. We analyzed genes that are a minimum of 1 kb in length from +1 nucleosome to TTS and used a bed file that contains only the top 20% of wild-type HSV-Chd1 occupied genes and sorted by maximum HSV-Chd1 occupancy (as described in ChIP-seq data analysis) ($n = 784$ genes). To generate metaplots for each genotype, the matrix obtained from deepTools computeMatrix containing data from 200 bp upstream of the +1 nucleosome, called from [113], and 1 kb beyond in 5 bp bins (240 bins total) was loaded into RStudio version 2022.7.1.554. Data for +1 to +4 nucleosomes were subset into 30 bins (where each bin is 5 bp). The nucleosome center was defined by calling the five-maximum consecutive bins for each 30 bin nucleosome subset (+1 through +4) with the middle bin selected as the center point. Metaplots of these data were generated in GraphPad Prism 10 with the nucleosome centers displayed as vertical lines for wild type (black) or mutant (indicated color).

CUT&RUN analysis

Fastq files were trimmed to 25 bp using an awk command. Integrity of sequencing data was verified by fastqc version 0.11.9. Reads were aligned to the *M. musculus*

(mm10) and *D. melanogaster* (dm6) genomes using bowtie2 version 2.4.5 with parameters -I 10 -X 1000 -N 1 –very-sensitive for paired end-sequencing [108]. Low quality reads were filtered using Picard version 2.5.0 and filtered for mapping quality (MAPQ ≥ 10) using SAMtools version 1.14 [109]. Reads were counted with SAMtools version 1.14 flagstat. Datasets were computationally size selected using SAMtools, with 130–500 bp for CHD1 and 150–500 bp for H3K4me3 and H3K36me3. For H3K4me3 and H3K36me3, normalized bigwigs were generated using bamcoverage [111] with parameters –centerReads –binSize 5 –scaleFactor x, where the scaling factor was determined for each sample using *Drosophila* reads [114]. For CHD1 CUT&RUN, normalized bigwigs were generated using bamcoverage [111] with parameters –centerReads –binSize 5 –normalizeUsing RPGC –effectiveGenomeSize 2308125349. Normalized bigwigs for three or four replicates were averaged using WiggleTools and the 'mean' function [112]. Browser tracks were generated from merged bigwig files using IGV genome browser. Published mES cell CHD1 ChIP-seq data (SRR1747927/SRR1747928) were subset to identify the top quintile of Chd1-bound genes and plotted with deepTools computeMatrix and plotHeatmap. Published mES cell MNase-seq data (SRR1265799) was used to compare profiles, with normalized bigwigs generated using bamcoverage [111] with parameters –centerReads –binSize 5 –normalizeUsing RPGC –effectiveGenomeSize 2308125349. To generate metaplots, the output of deepTools plotProfile containing binned data (10 bp) from TSS to 2 kb or −1 kb to +2 kb. Output from plotProfile was plotted in GraphPad Prism 10 to generate final metaplots. The mm10 Encode Blacklisted regions were also excluded from the normalized bigwigs. Information on replicates is provided in the Supplementary data file.

ATAC-seq analysis

ATAC-seq data quality was verified with Pepatac version 0.10.3 [115]. Pepatac parameters were: -Q paired -M 90G –aligner bowtie2 –trimmer trimmomatic –deduplicator picard –peak-caller macs2 –peak-type fixed -G mm10 -P 24 -R [115]. De-duplicated bam files obtained from Pepatac were shifted for ATAC-seq analysis using the deepTools alignmentSieve function using alignmentSieve –ATACshift [111]. Resulting bam files were then size-selected into accessible fragments (length 1–100 bp) or mononucleosome-sized fragments (length 180–247 bp) using deepTools bamCoverage with settings –normalizeUsing RPGC –effectiveGenomeSize 2652783500 –MNase –binSize 1 –extendReads and by removing the mm10 Encode Blacklisted regions [106]. Normalized bigwigs for three to four replicates were averaged using WiggleTools and the 'mean' function [112]. Published CHD1 ChIP-seq datasets and an mES cell MNase-seq dataset were used as described in the CUT&RUN analysis section. Output from plotProfile was plotted in GraphPad Prism 10 to generate final metaplots. NucleoATAC was used to call nucleosomes in wild type replicates [116]. NucleoATAC-called nucleosomes from two or more wild-type replicates were then selected. Nucleosomes over all genes or CHD1 top quintile occupied genes were subset using bedtools intersect and used to assess mononucleosome ATAC-seq enrichment in wild type and mutant cell lines. MNase-seq data are overlayed as a control for nucleosome enrichment at these sites. Information on replicates is provided in the Supplementary data file.

Data reproducibility

All sequencing experiments were performed for 2–5 biological replicates with replicate information provided in the Supplementary data file. Yeast ChIP-seq experiments were spiked-in with *S. pombe* chromatin for data normalization. H3K4me3 and H3K36me3 CUT&RUN experiments were spiked-in with batch-controlled *Drosophila* nuclei. For all experiments on mutant strains or cell lines, wild-type samples were grown and processed in parallel to minimize batch effects. Pearson correlation values are reported for all sequencing experiments in the Supplementary data file. Western blot, indirect immunofluorescence, ChIP-qPCR, and Y2H experiments were performed in biological triplicate. The BPA crosslinking experiment was performed four independent times. Error bars for ChIP-qPCR represent standard deviation with unpaired *t*-tests comparing wild-type to mutant strains.

Reagents

See the Supplementary data file.

Biological resources

See Supplementary Table S1 for a list of yeast strains and the Supplementary data file for mouse ES cell lines.

Statistical analyses

See figure legends and the Materials and methods section.

Novel programs, software, and algorithms

Not applicable.

Web sites/data base referencing

See the Supplementary data file.

Results

An N-terminal region of Rtf1 is sufficient to interact with the Chd1 CHCT domain

We previously found that amino acids 863–1468 of *S. cerevisiae* Chd1 can interact with full-length Rtf1 in a Y2H, but an Rtf1 derivative lacking amino acids 3–30 cannot support this interaction [19, 76]. To determine the region of Rtf1 sufficient for its interaction with Chd1, we performed a Y2H experiment with the GAD-Chd1(863–1468) construct, a series of GBD-Rtf1 constructs, and a yeast strain containing a *GAL1p-HIS3* reporter gene (Supplementary Fig. S1A) [79]. We observed interaction between GAD-Chd1(863–1468) and full-length GBD-Rtf1, GBD-Rtf1(1–184), and GBD-Rtf1(1–30) as indicated by growth on -His medium or -His medium supplemented with 3-AT, a competitive inhibitor of the His3 enzyme, to elevate the stringency of the assay (Supplementary Fig. S1A). Empty vector (EV) controls showed that both Rtf1 and Chd1 are required for growth on the test media except for the GBD-Rtf1(1–30) construct, which supported growth on -His medium even in the presence of the GAD EV (Supplementary Fig. S1A). Addition of 3-AT eliminated the background signal from GBD-Rtf1(1–30), allowing us to observe interactions between GBD-Rtf1(1–30) and GAD-Chd1(863–1468) or additional Chd1 constructs (below).

Chd1(863–1468) contains the Chd1 DBD, the CHCT domain, and an intervening disordered region (Fig. 1A). We hypothesized that the CHCT domain may be required for the

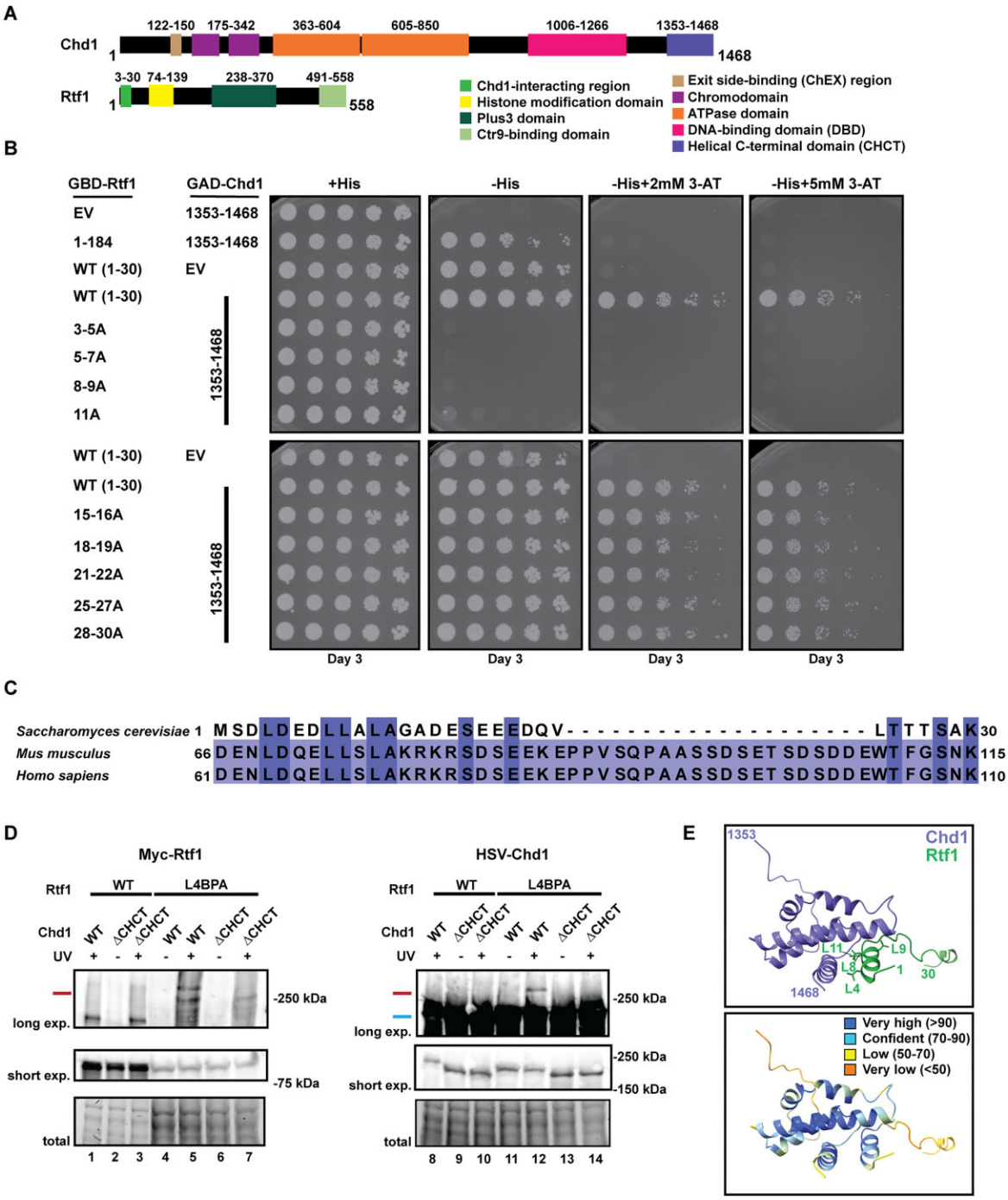

Figure 1. The Rtf1 N-terminal region directly interacts with the Chd1 CHCT domain (**A**) Diagrams of *S. cerevisiae* Chd1 and Rtf1 with domains indicated [32–34, 38, 63,74, 76, 140]. (**B**) Yeast two-hybrid (Y2H) analysis of the *S. cerevisiae* Rtf1 N-terminal region and the Chd1 CHCT domain. Plasmids expressing Gal4 DNA-binding domain (GBD)-Rtf1(1–30) with wild-type sequence or the indicated alanine substitutions were co-transformed with a plasmid expressing Gal4 activation domain (GAD)-Chd1(1353–1468). GBD-Rtf1(1–184), which does not activate the *GAL1p-HIS3* reporter on its own, was included as a control. EV = empty GBD or GAD vector as indicated. Cells were plated on indicated media and imaged after 3 days of growth ($n = 3$). (**C**) Multiple sequence alignment of the *S. cerevisiae* Rtf1 N-terminal region aligned to mouse and human RTF1. (**D**) *In vivo* photo-crosslinking of Rtf1-L4BPA with Chd1. Cells expressing Rtf1 and Chd1 derivatives were exposed to longwave ultraviolet (UV) light (+) or untreated (−) and then processed for western blot analysis using anti-Rtf1 antisera to detect Myc-tagged Rtf1 and HSV antibody to detect Chd1 derivatives (wild type = WT; C-terminally truncated Chd1 lacking amino acids 1353–1468 = ΔCHCT). The red bars indicate the Rtf1-L4BPA∼Chd1 crosslinked product (lanes 5 and 12). The blue bar indicates Chd1. The panels are from the same membrane that was cut, probed with the indicated antibody, and realigned prior to imaging. Short exposures show levels of uncrosslinked Rtf1 and Chd1 in the extracts. For visualizing Myc-Rtf1, lanes 1–3 were loaded with five-fold less extract to compensate for the higher levels of full-length Myc-Rtf1 in WT strains compared to those produced by amber codon suppression in lanes 4–7. Lanes 4–14 were loaded with equivalent amounts of extract. Total protein levels were measured using Bio-Rad Stain-Free imaging technology to serve as a loading control. (**E**) AlphaFold 3 analysis of the predicted interaction between the Rtf1 N-terminal region [1–30] and the Chd1 CHCT domain (1353–1468) [97]. Top: Chd1 and Rtf1 are colored purple and green, respectively. Rtf1 amino acids important for the Rtf1–Chd1 interaction by photo-crosslinking or Y2H are indicated. Bottom: Visualization of predicted local distance difference test (pLDDT) scores, assessing confidence in the AlphaFold model. Root mean square deviation (RMSD) of the predicted yeast CHCT structure relative to the human CHCT NMR structure = 1.041 Å).

Rtf1–Chd1 interaction and created a GAD-Chd1(1353–1468) construct. In this Y2H experiment, GAD-Chd1(1353–1468) is sufficient to support an interaction with GBD-Rtf1(1–184) or GBD-Rtf1(1–30) (Fig. 1B), demonstrating that the Chd1 CHCT is the domain interacting with Rtf1.

To identify the amino acids in Rtf1 required for its interaction with Chd1, we performed an alanine substitution screen across Rtf1(1–30) and tested for interaction with Chd1(1353–1468) by Y2H (Fig. 1B and C). Substitutions 3–5A, 5–7A, 8–9A, and 11A in the Rtf1(1–30) construct greatly reduced the interaction with GAD-Chd1(1353–1468) (Fig. 1B), whereas substitutions 15–16A, 18–19A, 21–22A, 25–27A, and 28–30A had little to no effect. Similar results were observed with the Chd1(863–1468) construct (Supplementary Fig. S1B). Control experiments with EVs confirmed the specificity of the interactions (Supplementary Fig. S1C). In addition to eliminating the interaction with Chd1(1353–1468), the 3–5A, 5–7A, 8–9A, and 11A substitutions eliminated the low level of activation by Rtf1(1–30), which was evident on -His medium lacking 3-AT (Supplementary Fig. S1C). Deletion of the *CHD1* gene in the Y2H strain did not eliminate activation by Rtf1(1–30) alone; therefore, the source of this phenotype remains unclear (Supplementary Fig. S1D). Western blot analysis confirmed expression of GBD-Rtf1(1–30) and the mutant derivatives as well as GAD-Chd1(863–1468) and GAD-Chd1(1353–1468) (Supplementary Fig. S1E–G). Together, these data demonstrate an interaction between the Chd1 CHCT domain and amino acids 1–30 of Rtf1.

Site-specific protein crosslinking demonstrates a direct physical interaction between Rtf1 and Chd1 *in vivo*

Multiple sequence alignment of the Rtf1 N-terminus revealed a patch of conserved amino acids that are shared between yeast, mouse, and human, including yeast residues L4, D5, L8, L9, and L11 that are required for the Rtf1–Chd1 interaction (Fig. 1B and C). We termed this region the "LLALA box" after the yeast sequence. Using a system for site-specifically incorporating an unnatural amino acid within a protein of interest through amber codon suppression [117], we replaced Rtf1 L4 with the crosslinking competent, photo-reactive phenylalanine analog BPA to test for a direct interaction with Chd1 *in vivo*. Western blot analysis showed a super-shifted UV-dependent product with Myc-Rtf1 L4BPA that was visible when probing for either Rtf1 or HSV-tagged Chd1, which was expressed from the endogenous locus (Fig. 1D, lanes 5 and 12). We generated a strain containing an integrated *HSV-chd1ΔCHCT* mutation by deleting the sequence encoding amino acids 1353–1468 of HSV-Chd1 through homologous recombination. The Rtf1–Chd1 interaction is dependent on the Chd1 CHCT domain, as the ΔCHCT mutant did not yield a photo-crosslinked product with Rtf1 L4BPA (Fig. 1D, lanes 7 and 14). Therefore, the Rtf1–Chd1 interaction is direct and requires Rtf1 L4 and the Chd1 CHCT.

We used AlphaFold 3 to model the interaction between the Rtf1 N-terminal region (1-30) and the Chd1 CHCT domain (1353–1468) and assess confidence in the model through pLDDT scores and a PAE plot [97] (Fig. 1E and Supplementary Fig. S1H). The Rtf1 N-terminal region, which is not visible in existing structures of Rtf1 [53, 118, 119], is predicted to fold into an alpha helix in which L4, L8, and L11 face the C-terminal helix of the CHCT domain (Fig. 1E). Thus, Rtf1 amino acids important for the Rtf1–Chd1 interaction as measured by Y2H and *in vivo* photo-crosslinking are predicted to interface with the CHCT domain.

Rtf1 regulates the distribution of Chd1 on active genes

To determine the effects of mutating the Rtf1–Chd1 interface on protein localization and chromatin structure *in vivo*, we generated yeast strains expressing integrated, epitope-tagged derivatives of HSV-Chd1 and HA-Rtf1. We first tested if the tags alter the functions of the wild-type proteins using the *GAL1p-FLO8-HIS3* reporter for cryptic transcription initiation [9]. Upon changes to local chromatin structure, an otherwise cryptic transcription initiation site within the *FLO8* sequence can become accessible, resulting in a *FLO8-HIS3* fusion transcript that supports growth on SC-His + gal medium [9, 120]. While *chd1*Δ and *rtf1*Δ strains harboring the reporter show the expected His^+ phenotypes [9], the HSV-Chd1 and HA-Rtf1 strains are phenotypically wild type in this assay (Supplementary Fig. S2A). Based on the Y2H results (Fig. 1B), multiple sequence alignment (Fig. 1C), and AlphaFold 3 prediction (Fig. 1E), we focused on conserved residues in the LLALA box that are responsible for supporting the Rtf1–Chd1 interaction and generated strains expressing HA-Rtf1(8–9A) and HA-Rtf1(11A) from the endogenous *RTF1* locus. Western blot analysis showed that levels of the HA-Rtf1(8–9A), HA-Rtf1(11A), and HSV-Chd1ΔCHCT proteins are similar to wild-type controls (Fig. 2A). To test if deletion of the CHCT domain altered the subcellular localization of Chd1, we performed indirect immunofluorescence. Both HSV-Chd1 and HSV-Chd1ΔCHCT co-localized with DAPI staining, demonstrating that nuclear localization of Chd1 is retained in the HSV-Chd1ΔCHCT strain (Supplementary Fig. S2B).

To determine the genome-wide impact of the Rtf1–Chd1 interaction on the chromatin occupancy of Chd1, Rtf1, and RNA Pol II, we performed spike-in normalized ChIP-seq. As expected, wild-type HSV-Chd1 and HA-Rtf1 are enriched at highly transcribed genes, as defined by RNA Pol II occupancy levels (Fig. 2B) [18, 63]. To test if the Rtf1–Chd1 interaction affects the distribution of RNA Pol II, Rtf1, or Chd1, we examined the localization of these proteins in wild-type and HA-Rtf1(8–9A), HA-Rtf1(11A), HSV-Chd1ΔCHCT, *rtf1*Δ, and *chd1*Δ mutant strains, focusing on the top quintile of Chd1-occupied genes. Changes in protein distribution were assessed by calculating the position of maximum protein occupancy (Fig. 2C–E). Relative to wild type, the patterns of RNA Pol II and HA-Rtf1 occupancy were only modestly affected in the mutant strains (Fig. 2C and D). In contrast, we observed a marked 5′ shift in the position of maximum HSV-Chd1 occupancy in the HA-Rtf1(8–9A), HA-Rtf1(11A), and HSV-Chd1ΔCHCT strains at genes sorted into two different length classes (Fig. 2E and Supplementary Fig. S3A). Interestingly, a more moderate shift in HSV-Chd1 occupancy was observed in the *rtf1*Δ strain compared to the Rtf1–Chd1 interaction mutants. Browser tracks of HSV-Chd1 chromatin occupancy over *YEF3*, *CDC19*, and *PMA1* exemplify the patterns observed genome-wide (Fig. 2F). The 5′ shift of HSV-Chd1 occupancy in the Rtf1–Chd1 interaction mutants is also evident when ChIP-seq data are plotted for all genes or without spike-in normalization (Supplementary Fig. S3B and C). To determine if the shift in Chd1 occupancy correlates with

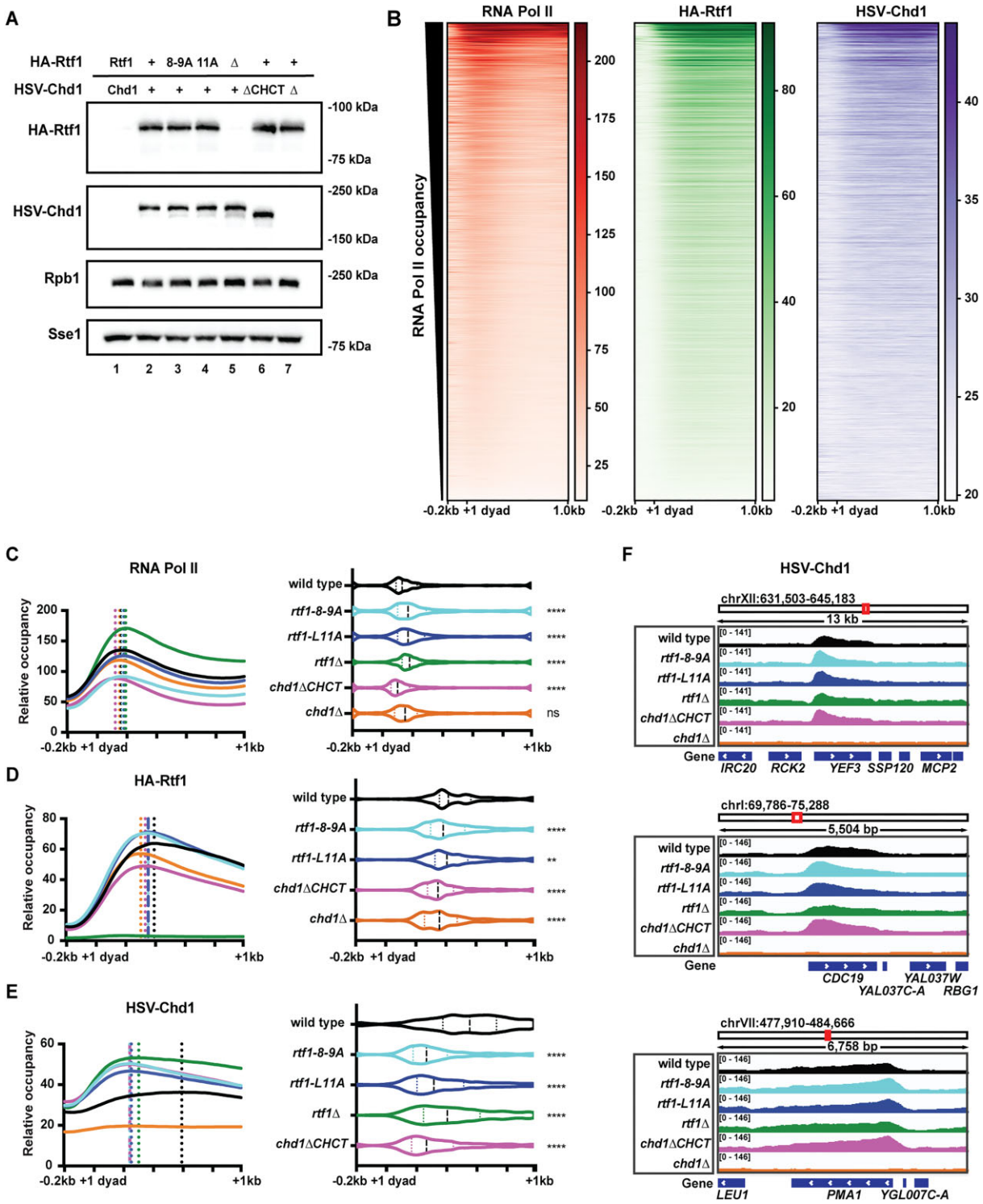

Figure 2. Chd1 distribution across genes is dependent on its interaction with Rtf1 (**A**) Western blot analysis of HA-Rtf1, HSV-Chd1, and Rpb1 levels in strains expressing the indicated HA-Rtf1 and HSV-Chd1 proteins (lanes 2–7; + indicates wild-type tagged protein). In lane 1, extract from an untagged wild-type strain was used as a control. Samples in lanes 5 and 7 were prepared from strains deleted of *RTF1* or *CHD1*, respectively. 8WG16 antibody was used to detect Rpb1. Sse1 served as a loading control. (**B**) Heatmap representations of spike-in normalized RNA Pol II (8WG16), HA-Rtf1, and HSV-Chd1 ChIP-seq data in wild type, sorted by RNA Pol II occupancy for genes over 1 kb in length spanning from 200 bp upstream of the +1 nucleosome dyad to 1 kb downstream ($n = 3919$ genes). (**C**) Metaplot of average RNA Pol II ChIP-seq signal over the top 20% HSV-Chd1 occupied genes as determined from the wild-type dataset (minimum of 1 kb in length after +1 dyad, $n = 784$ genes). Dotted vertical lines show the point of maximum RNA Pol II occupancy for indicated strains (left). Violin plot representing the distribution of the point of maximum RNA Pol II occupancy for every gene with median and interquartile ranges shown (right). Wilcoxon rank sum test was used to compare each strain to wild type: $P < .05$ (*), $P < .01$ (**), $P < .001$ (***), and $P < .0001$ (****). The average of 2–5 biological replicates for each strain is shown. Information on replicates is provided in the Supplementary data file. (**D**) As in panel (C), but for HA-Rtf1 ChIP-seq signal ($n = 784$ genes). The average of 2–5 biological replicates for each strain is shown. (**E**) As in panel (C), but for HSV-Chd1 ChIP-seq signal ($n = 784$ genes). The average of 2–4 biological replicates for each strain is shown. (**F**) Integrative Genomics Viewer (IGV) browser tracks of HSV-Chd1 ChIP-seq signal for genes *YEF3*, *CDC19*, and *PMA1*.

gene expression level, we quantified the ratio of HSV-Chd1 occupancy at the 5′ end relative to the 3′ end of each gene and plotted this ratio against RNA Pol II occupancy levels across gene bodies (Supplementary Fig. S3D). Compared to wild type, we observed an increased correlation between the 5′/3′ HSV-Chd1 occupancy ratio and RNA Pol II occupancy in the *chd1ΔCHCT* mutant, suggesting that the 5′ shift in Chd1 occupancy in the mutant is related to transcriptional activity.

We performed ChIP-qPCR to verify the ChIP-seq results and found that the HA-Rtf1(8-9A) and HA-Rtf1(11A) substitutions caused significantly increased HSV-Chd1 occupancy at the 5′ end of *YEF3* and decreased HSV-Chd1 occupancy at the 3′ ends of *YEF3* and *CDC19* (Supplementary Fig. S3E). HSV-Chd1ΔCHCT occupancy was significantly reduced at the 3′ ends of *CDC19* and *YEF3* (Supplementary Fig. S3E). Further, *rtf1*Δ led to reduced HSV-Chd1 occupancy at both the 5′ and 3′ ends of *CDC19*, consistent with previous results (Supplementary Fig. S3E) [76]. Similar trends, though modest, were observed at *PMA1* (Supplementary Fig. S3E). ChIP-qPCR at the same loci revealed no significant changes in HA-Rtf1 chromatin occupancy, except for a modest reduction in HA-Rtf1(11A) at the 3′ end of *CDC19* (Supplementary Fig. S3F). Together, these results demonstrate the importance of the Rtf1 LLALA box and the Chd1 CHCT domain in regulating Chd1 distribution across active genes in yeast.

Disruption of the Rtf1–Chd1 interaction causes cryptic intragenic transcription

Chd1 is required for the regular spacing of nucleosomes across genes [3, 5, 6, 121, 122]. Therefore, we hypothesized that disruption of the Rtf1–Chd1 interaction, required for proper Chd1 localization, would result in cryptic transcription initiation and altered nucleosome positioning. We tested the Rtf1 LLALA box mutants for cryptic transcription using the *GAL1p-FLO8-HIS3* reporter. When expressed from plasmids, HA-Rtf1, but not the HA-Rtf1Δ3–30, 3–5A, 5–7A, 8–9A, and 11A derivatives, complemented the cryptic transcription phenotype of an *rtf1*Δ strain (Supplementary Fig. S4A). HA-Rtf1 protein levels were similar in these transformed strains (Supplementary Fig. S4B). Similarly, the integrated Rtf1–Chd1 interaction mutants, expressing HA-Rtf1(8–9A), HA-Rtf1(11A), and HSV-Chd1ΔCHCT from endogenous loci, exhibited a cryptic transcription initiation phenotype (Fig. 3A). Notably, while *chd1*Δ causes the strongest phenotype in this assay, the cryptic initiation phenotypes of the HA-Rtf1(8–9A), HA-Rtf1(11A), and HSV-Chd1ΔCHCT mutants appear more severe than that of the *rtf1*Δ strain (Fig. 3A). Together with our ChIP-seq results (Fig. 2), this observation shows that complete loss of Rtf1 has a different effect than loss of the Rtf1–Chd1 interaction alone and suggests that the presence of other Rtf1 functions in the *rtf1* point mutants contributes to the strength of the mutant phenotypes.

The Rtf1–Chd1 interaction is required for proper nucleosome positioning over Chd1-occupied genes

To determine if the Rtf1–Chd1 interaction is important for maintaining chromatin structure across genes, we performed MNase-seq on HA-Rtf1(8–9A), HA-Rtf1(11A), HSV-Chd1ΔCHCT, *rtf1*Δ, and *chd1*Δ strains without performing any experimental size selection to enrich for fragments. Relative to wild type, nucleosome positioning is disrupted in all mutants over Chd1-occupied genes (Fig. 3B and C and Supplementary Fig. S4C). To quantify changes in mononucleosome positions, we calculated the nucleosome center point for the +1 to +4 nucleosomes over the average of Chd1-occupied genes (top quintile, Fig. 3C). The nucleosomes in the Rtf1–Chd1 interaction mutants were consistently shifted 5′. We observed a similar 5′ shift in nucleosomes when we plotted these data over the TSS of all genes (Supplementary Fig. S4C). Beyond the +4 nucleosome, positioning was severely impacted such that nucleosome locations could not be reliably identified in these strains. In contrast with the Rtf1 point mutants and the Chd1ΔCHCT mutant, the *rtf1*Δ strain showed more modest changes to nucleosome positions, suggesting that substitutions in the Rtf1 LLALA box separate the effect of Chd1 interaction from other Rtf1 functions. These data are in line with the *rtf1*Δ HSV-Chd1 ChIP-seq data, which showed a less pronounced upstream shift of Chd1 (Fig. 2E). Similarly, the *chd1*Δ mutant had near wild-type positions at the first three nucleosomes, but a clear loss of nucleosome positioning at and beyond the +4 nucleosome (Fig. 3C), consistent with prior studies [3, 5, 6].

Nucleosome remodeling by Chd1 across gene bodies is partially redundant with nucleosome remodeling by the Isw1 ATPase, as *isw1*Δ *chd1*Δ double mutants exhibit enhanced changes in genic chromatin structure relative to single mutants [3, 5, 6, 123]. Therefore, we hypothesized that the altered nucleosome positioning observed in Rtf1–Chd1 interaction mutants would be exaggerated when paired with *isw1*Δ. At Chd1-occupied genes, *isw1*Δ led to 5′ shifting of nucleosomes, particularly at the +3 and +4 positions (Fig. 3D). Deletion of *ISW1* in the HA-Rtf1(8-9A), HA-Rtf1(11A), and HSV-Chd1ΔCHCT strains caused a greater disruption of chromatin structure than observed in the single mutants with 5′ shifts of nucleosomes and near complete loss of nucleosome peaks beyond the +2 position (Fig. 3C and D). Nucleosome positioning was also disrupted in the *isw1*Δ *rtf1*Δ double mutant. These results show that disruption of the Rtf1–Chd1 interaction alters nucleosome positioning across gene bodies likely due to altered Chd1 distribution resulting in improper spacing of nucleosomes.

A recent study demonstrated gene-body enrichment of hexasome–nucleosome complexes (also referred to as overlapping dinucleosomes or OLDNs [124]) and dinucleosomes in yeast strains lacking both Chd1 and Isw1 [51]. By focusing on different fragment size classes in our MNase-seq data, we assessed the effects of disrupting the Rtf1–Chd1 interaction on the accumulation and localization of hexasome–nucleosome complexes, dinucleosomes, and sub-nucleosome particles (Supplementary Fig. S4D). Deletion of *CHD1*, in the presence or absence of Isw1, led to a 5′ shift of hexasome–nucleosome complexes and dinucleosomes at the 5′ ends of genes, relative to wild type (Fig. 3E and Supplementary Fig. S4E and F). Disruption of the Rtf1–Chd1 interface by deletion of the Chd1 CHCT domain or substitutions in the Rtf1 LLALA box similarly caused 5′-shifting of hexasome–nucleosome complexes and dinucleosomes to a degree greater than deletion of *RTF1*. In addition, we qualitatively observed an enrichment of the first and second hexasome–nucleosome complexes relative to the third and fourth hexasome–nucleosome complexes in the Rtf1–Chd1 interaction mutants, and this enrichment is not observed in the wild-type strain (Fig. 3E). While dinucleosomes and hexasome–nucleosome complexes show a distinct pattern rel-

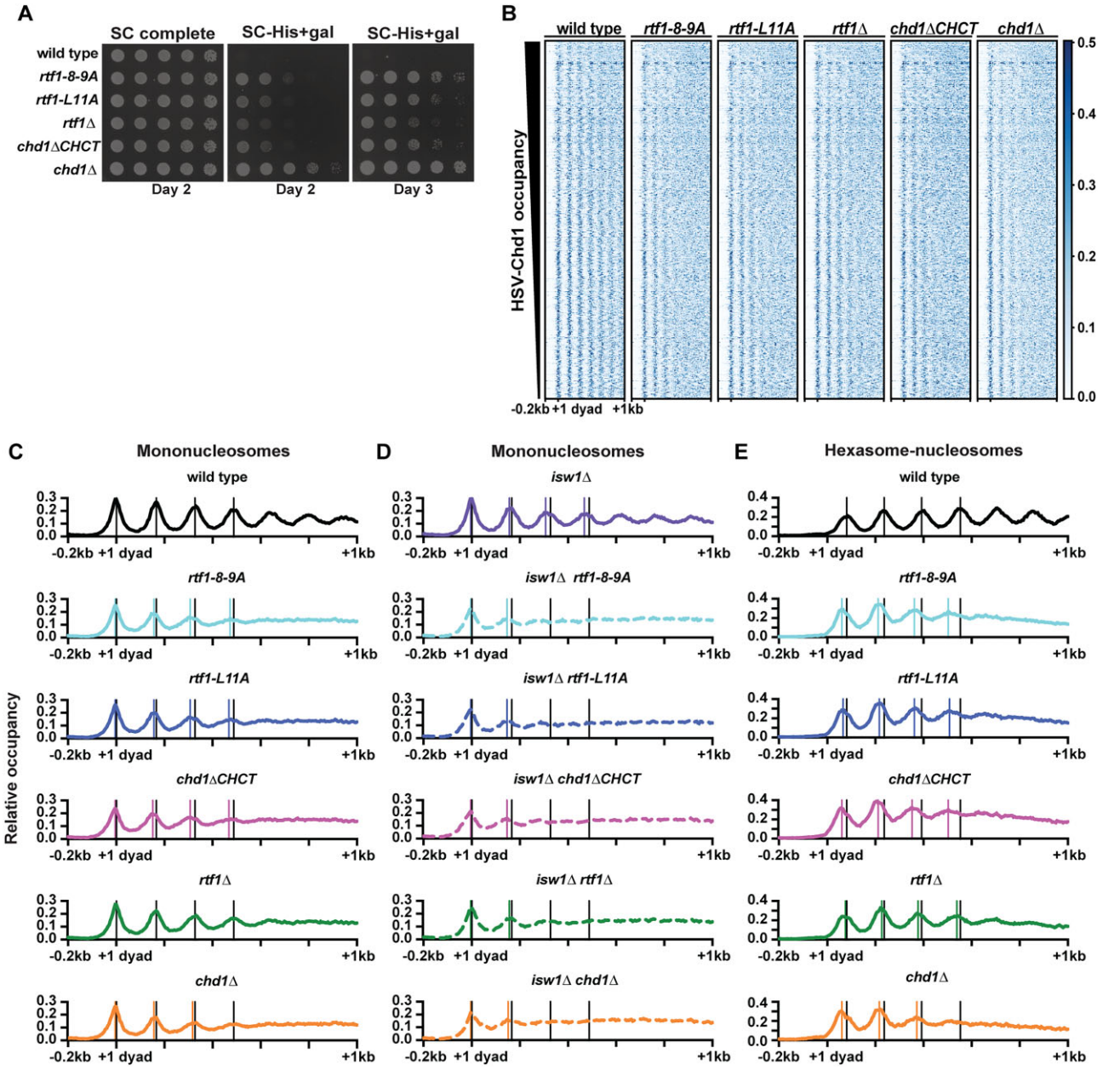

Figure 3. The Rtf1–Chd1 interaction is required for proper nucleosome positioning across Chd1-occupied genes (**A**) Analysis of cryptic transcription initiation phenotypes of Rtf1–Chd1 interaction mutants using the *GAL1p-FLO8-HIS3* reporter [9]. Images were taken on the indicated days after plating ($n = 3$). (**B**) Heatmap representation of mononucleosome positions (137–157 bp fragment sizes) determined by MNase-seq over the top 20% of HSV-Chd1-occupied genes as determined from the wild-type dataset (minimum of 1 kb in length, $n = 784$). Genes are sorted by HSV-Chd1 occupancy. (**C**) Metaplots of average MNase-seq signal for the genes analyzed in panel (B). Black and colored vertical lines denote the calculated mononucleosome center points of the +1 through +4 nucleosomes in wild-type and mutant strains, respectively. Where no colored lines are shown, no nucleosome shift was observed at that position in mutant strains or a nucleosome center point could not be called. Data were divided into 5-bp bins across the region of −0.2 kb to +1 kb relative to the +1 nucleosome dyad, as previously defined [113]. Information on replicates is provided in the Supplementary data file. (**D**) Metaplots of MNase-seq data for mononucleosome positions in *isw1*Δ and indicated double mutant strains as in panel (C). The nucleosome center points for the +3 and +4 nucleosomes in double mutant strains were unable to be calculated. (**E**) Metaplots of hexasome–nucleosome complex (230–270 bp fragment sizes) positions determined from MNase-seq data. Black and colored vertical lines denote the calculated hexasome–nucleosome complex center points in wild-type and mutant strains, respectively. The center point for the +4 hexasome–nucleosome complex in *chd1*Δ was unable to be calculated.

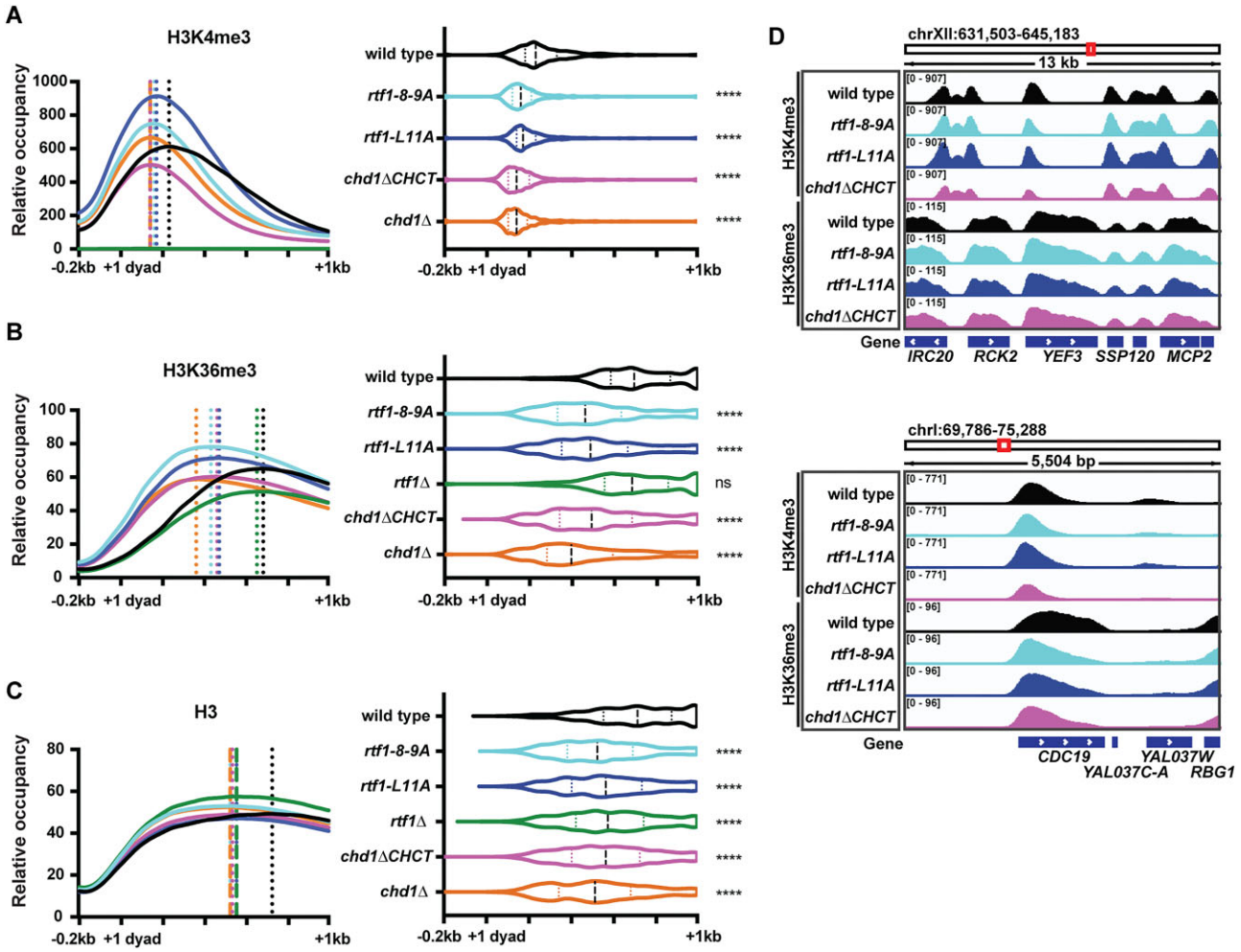

Figure 4. The Rtf1–Chd1 interaction is required for proper localization of modified histones across gene bodies (**A**) Metaplot of average spike-in normalized H3K4me3 ChIP-seq data from wild-type, *rtf1-8-9A*, *rtf1-L11A*, *rtf1*Δ, *chd1*Δ*CHCT*, and *chd1*Δ strains over the top 20% of HSV-Chd1-occupied genes (determined from the wild-type dataset, minimum of 1 kb in length after +1 dyad, $n = 784$ genes) where dotted vertical lines show the maximum point of factor occupancy for each strain (left). The green line represents *rtf1*Δ data. Violin plot representing maximum point of factor occupancy for each individual gene; median and interquartile ranges for the data are shown (right). Wilcoxon rank sum test was used to compare each strain to wild type: $P < .05$ (*), $P < .01$ (**), $P < .001$ (***), and $P < .0001$ (****). Data are averaged from 2–5 biological replicates. Information on replicates can be found in the Supplementary data file. (**B**) As in panel (A), for H3K36me3 ChIP-seq. Data are averaged from 2–3 biological replicates. (**C**) As in panel (A), for H3 ChIP-seq. Data are averaged from 2–3 biological replicates. (**D**) IGV browser tracks of H3K4me3 and H3K36me3 ChIP-seq signals over *YEF3* and *CDC19* in the indicated strains.

ative to mononucleosomes, subnucleosome positions generally reflect changes observed in mononucleosome positions in the presence or absence of Isw1 (Supplementary Fig. S4G). These results demonstrate that the Rtf1–Chd1 interaction is required for the appropriate positioning and resolution of multiple classes of nucleosome particles across gene bodies, and changes to all these particles are enhanced when mutations disrupting the Rtf1–Chd1 interaction are combined with *isw1*Δ.

Transcription-coupled histone modifications are shifted upstream upon loss of the Rtf1–Chd1 interaction

Histone post-translational modifications, including H3K4me3 and H3K36me3, are distributed across gene bodies at levels that correlate with transcription [125]. Based on our finding that Chd1 occupancy is shifted 5′ with an associated shift in nucleosome positioning in Rtf1–Chd1 interaction mutants, we anticipated a concordant change in transcription-associated histone modifications. ChIP-seq analysis revealed an upstream shift of H3K4me3 and H3K36me3 in the Rtf1–Chd1 interaction mutants and the *chd1*Δ strain relative to wild-type locations at the top 20% of Chd1-occupied genes in two length classes (Fig. 4A and B and Supplementary Fig. S5A and B). A shift in the broad distribution of total H3 was also observed in the Rtf1–Chd1 interaction and *chd1*Δ mutants, consistent with the MNase-seq data (Fig. 4C and Supplementary Fig. S5C). In the *rtf1*Δ strain, H3K4me3 was detected at background levels as expected [76], while the H3K36me3 pattern was similar to that of the wild-type strain (Fig. 4A and B and Supplementary Fig. S5A and B). The 5′ shift in H3K4me3, H3K36me3, and H3 distribution observed over the top Chd1-occupied genes was also evident when all genes were examined (Supplementary Fig. S5D–F). The shift of H3K4me3, H3K36me3, and H3 in the *chd1*Δ strain agrees with previous results showing that Chd1 is required for their

proper distribution [10, 12]. Browser tracks for *YEF3* and *CDC19* exemplify the shift of H3K4me3 and H3K36me3 in the Rtf1 LLALA box and Chd1ΔCHCT mutants (Fig. 4D). Notably, western blot analysis demonstrated wild-type bulk levels of H3, H3K4me3, and H3K36me3 in the HA-Rtf1(8–9A), HA-Rtf1(11A), HSV-Chd1ΔCHCT, and *chd1*Δ mutants (Supplementary Fig. S5G). Therefore, mutations that disrupt the Rtf1–Chd1 interaction result in an upstream shift of transcription-coupled histone modifications.

Interaction of mouse RTF1 with CHD1 and CHD2 CHCT domains requires the RTF1 LLSLA box

The direct interaction between the Rtf1 N-terminal region and the Chd1 CHCT domain supports a mechanism by which yeast Rtf1 is required for proper distribution of Chd1 across genes, which in turn leads to appropriate nucleosome positioning and distribution of histone post-translational modifications. The Rtf1 residues required for this interaction are conserved in mouse and humans (Fig. 1C), suggesting that the Rtf1–Chd1 interaction may be conserved. CHD1 and CHD2 are the two mammalian CHD remodelers that are most similar to yeast Chd1, containing conserved domain architectures including CHCT domains (Fig. 5A and Supplementary Fig. S6A) [33]. To test for a potential interaction between RTF1 and CHD1 or CHD2, we conducted Y2H experiments with mouse RTF1, CHD1, and CHD2 proteins using constructs codon-optimized for expression in yeast. Mouse RTF1 contains a sequence similar to the yeast Rtf1 LLALA box, with a sequence change to LLSLA, a 65-amino acid extension N-terminal to the LLSLA box, and an insertion within the region that corresponds to yeast Rtf1(1–30) (Fig. 1C). Therefore, we designed several constructs: RTF1(1–321), RTF1(66–321) to eliminate the N-terminal extension, RTF1(1–115) to remove the histone modification domain (HMD) required for H2B ubiquitylation [63, 75, 76], and RTF1(66–95) which corresponds to yeast Rtf1(1–30) (Fig. 5B). For both CHD1 and CHD2, we designed two constructs: the CHCT domain alone and the CHCT domain with an N-terminal extension to the end of the DBD ("extended CHCT", Fig. 5B). As a positive control for the Y2H experiment, we included yeast Rtf1(1–184) and Chd1(1274–1468). EV controls paired with each mouse construct showed no growth on -His medium (Fig. 5C and Supplementary Fig. S6B). We found that RTF1(1–321) can interact with the CHCT domain alone or the extended CHCT of both CHD1 and CHD2 (Fig. 5C). RTF1(66–321) interacted with the CHD1 constructs and the CHD2 extended CHCT construct, although more weakly than RTF1(1–321), but did not interact with the CHD2 CHCT domain alone, suggesting that the first 65 amino acids in RTF1 are important for the interactions with CHD1 and CHD2. The smaller RTF1 (1–115) construct lacking the HMD was sufficient to interact with all CHD1 and CHD2 CHCT constructs; however, we did not observe interactions between RTF1 (66–95) and CHD1 or CHD2. These data demonstrate that the mouse RTF1 N-terminal region can interact with CHD1 and CHD2 via their CHCT domains.

To test if the mouse RTF1–CHD1 and RTF1–CHD2 interactions require the LLSLA box, we introduced alanine substitutions at the LLSL positions in the RTF1(1–321) and RTF1(1–115) constructs (Fig. 5D). Demonstrating the importance of the RTF1 LLSLA box for the interactions with CHD1 and CHD2, RTF1(1–115, AAAA) was no longer able to interact with any of the CHD1 or CHD2 CHCT constructs (Fig. 5E). We confirmed that levels of the GAD-CHD1 and GAD-CHD2 CHCT proteins were unaffected by the alanine substitutions in RTF1 and that the GBD-RTF1(1–115) and GBD-RTF1(1-115, AAAA) proteins were similarly expressed in the Y2H strains (Supplementary Fig. S6C and D). When the LLSLA box was mutated in the longer RTF1(1–321) construct, interactions between RTF1 and the extended CHCTs of CHD1 and CHD2 were partially retained, suggesting that sequences outside the LLSLA box also contribute to these interactions (Fig. 5E). Further supporting a conserved interaction between RTF1 and CHD1, we observed an LLSLA-dependent, cross-species Y2H interaction between mouse RTF1(1–115) and the yeast Chd1(863–1468) and Chd1(1353–1468) proteins (Supplementary Fig. S6E and F). However, we did not observe a Y2H interaction in the opposite direction, i.e. between yeast Rtf1(1–184) and the mouse CHD1 and CHD2 CHCT domain proteins. For RTF1(1–115) and CHD1(1378–1512), AlphaFold 3 predicted a top-scoring model in which the RTF1 helix harboring the LLSLA sequence interacts with the C-terminal helix of the CHD1 CHCT domain, similar to the prediction generated for the yeast Rtf1 and Chd1 proteins albeit at lower confidence (Supplementary Figs S6G and H). For RTF1(1–115) and CHD2(1432–1567), an interaction was predicted with only low confidence; however, a recent study focusing on a larger C-terminal fragment of mouse CHD2 reported an RTF1–CHD2 interaction by affinity purification/mass spectrometry supported by an AlphaFold Multimer model [126]. Together, these data suggest a conserved interaction between the N-terminal region of RTF1 and the CHD1 and CHD2 CHCT domains.

mRTF1-CHCT interaction mutations minimally affect chromatin structure in mES cells

Based on our Y2H results supporting a conserved interaction between mouse RTF1 and CHD1/2, we generated mES cell lines to test whether this interaction alters CHD1/2 distribution and chromatin structure across gene bodies. Using CRISPR/Cas9-directed homologous recombination, we generated cell lines encoding either alanine substitutions in the LLSLA box of RTF1, *rtf1(AAAA)*, or deleting the CHCT domains of CHD1 or CHD2 (*chd1*Δ*CHCT* and *chd2*Δ*CHCT*). By western blot analysis, we observed minimal changes in RTF1 abundance and the expected changes in the molecular weights of the CHD1ΔCHCT and CHD2ΔCHCT proteins (Fig. 6A). Notably, the levels of CHD1 and CHD2 were reduced in the *chd1*Δ*CHCT* and *chd2*Δ*CHCT* cell lines, respectively (Fig. 6A). To test whether the *chd1*Δ*CHCT* and *chd2*Δ*CHCT* mutations alter CHD1 or CHD2 chromatin occupancy, we performed CUT&RUN. While we were unable to obtain high quality CHD2 CUT&RUN datasets after testing three antibodies, we observed enrichment of CHD1 at the 5′ ends of genes in wild-type cells, as previously described using ChIP-seq (Fig. 6B and Supplementary Fig. S7A and B) [22]. In the *chd1*Δ*CHCT* cell lines, we observed a reduction in CHD1 occupancy likely due to reduced protein abundance. Due to the almost baseline levels of CHD1 in these cell lines, we were unable to robustly determine whether there is a shift in localization at the top quintile of CHD1-occupied genes (as defined from previous ChIP-seq datasets [22]) or over all genes (Fig. 6B and C and Supplementary Fig. S7A and B).

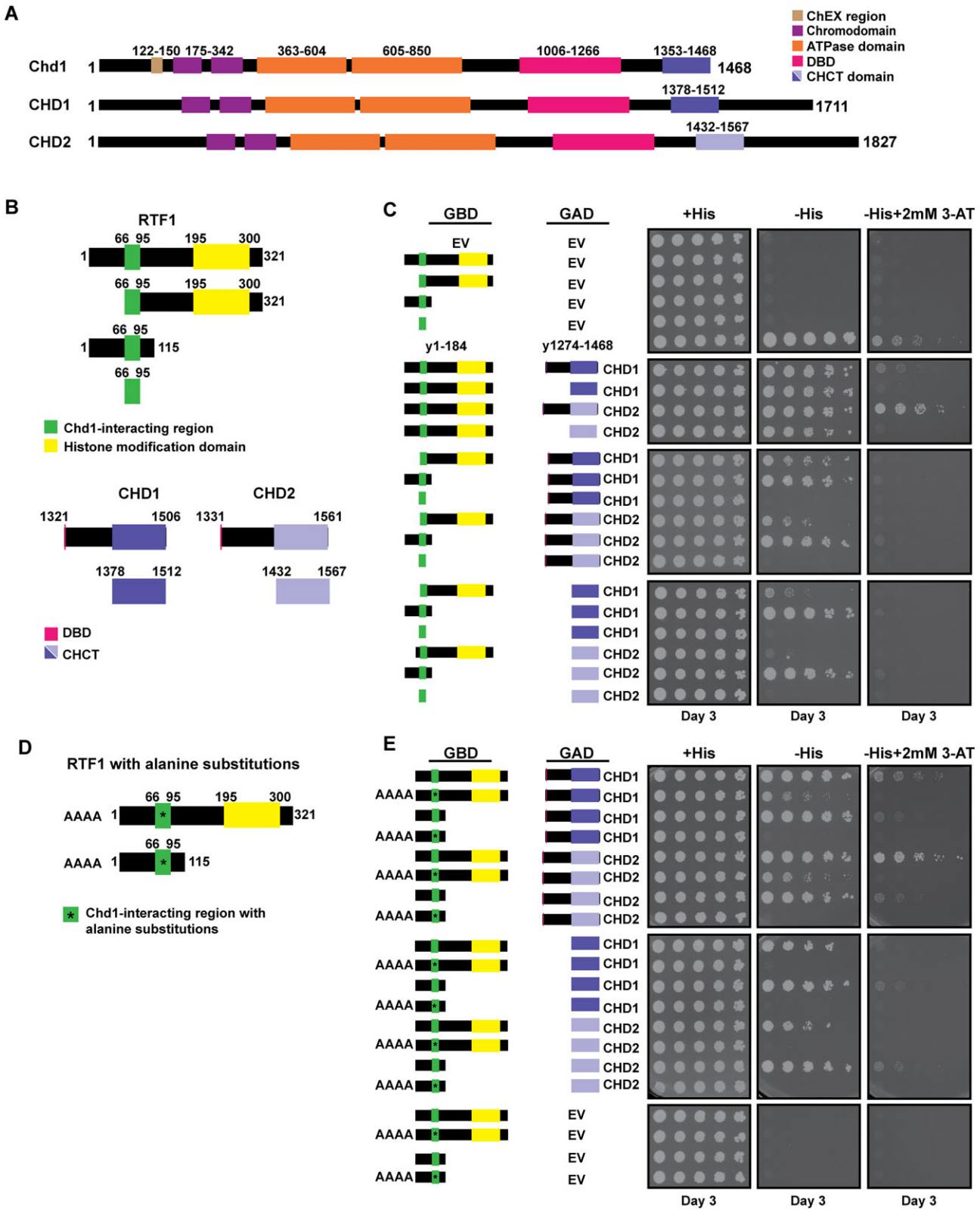

Figure 5. The N-terminus region of mouse RTF1 interacts with the CHCT domains of CHD1 and CHD2 in a LLSLA box-dependent manner (**A**) Domain organization of *S. cerevisiae* Chd1, mouse CHD1, and mouse CHD2. (**B**) Y2H constructs for mouse proteins RTF1, CHD1, and CHD2. Based on sequence conservation and experimental data in panel (C), the green and yellow boxes indicate positions of the CHD1-interacting region and HMD of mouse RTF1, respectively. (**C**) Y2H analysis of RTF1 with CHD1 or CHD2. Yeast GBD-Rtf1(1–184) and GAD-Chd1(1274–1468) are included as a positive control. ($n = 3$). (**D**) Y2H constructs with alanine substitutions at residues 73–76 within the RTF1 LLSLA box in the context of RTF1(1–321) or RTF1(1–115). (**E**) Y2H analysis of the interactions between wild-type and mutant RTF1 with CHD1 or CHD2 ($n = 3$).

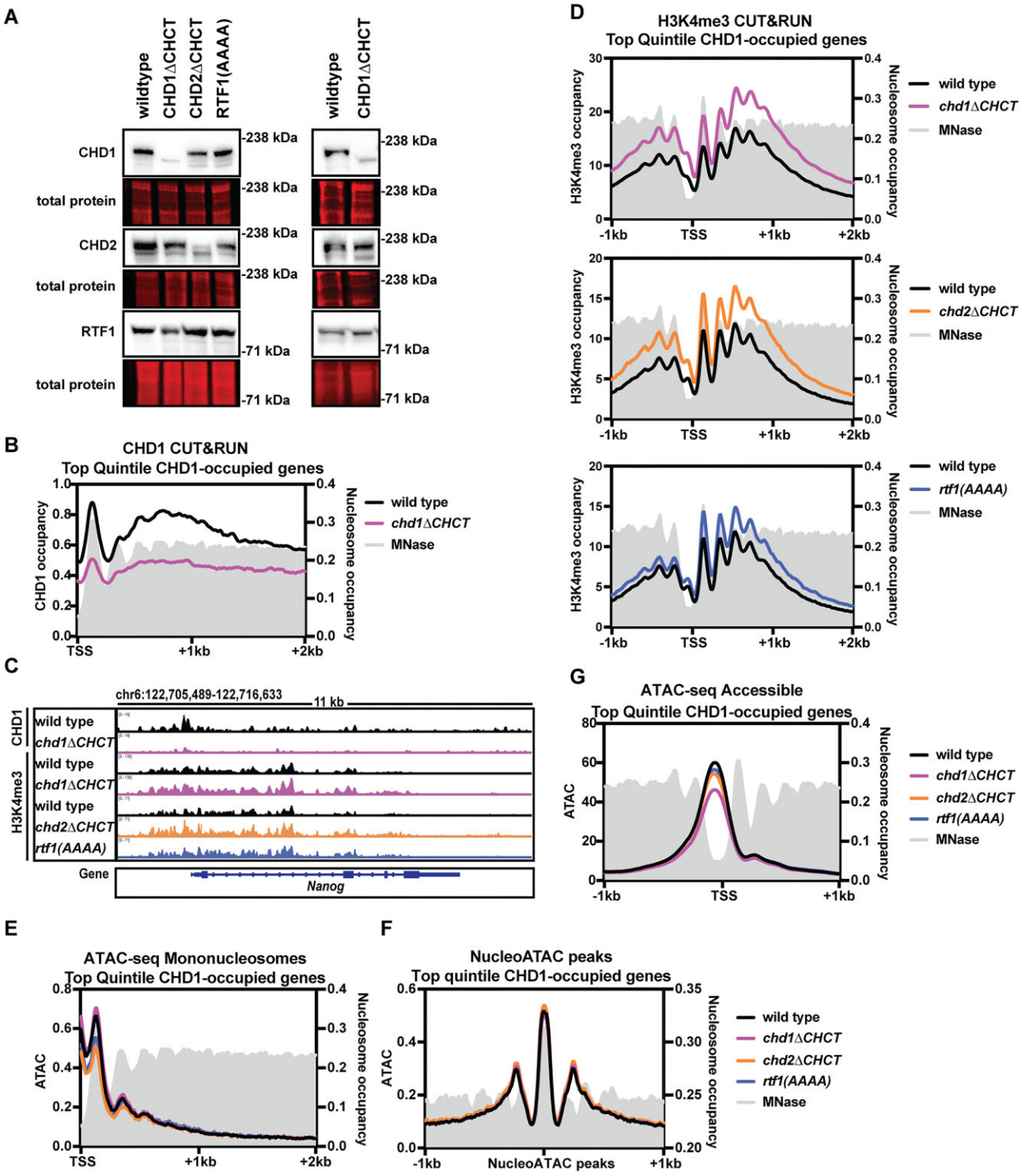

Figure 6. mES cell lines with mutations in the mRTF1–mCHD1/2 interacting regions have minimal changes in H3K4me3 and nucleosome positions (**A**) Western blot analysis for mouse CHD1, CHD2, and RTF1 in the indicated mES cell lines. Two independent CHD1ΔCHCT clones are shown. (**B**) Metaplot of average CHD1 CUT&RUN data in wild-type (black) and *chd1ΔCHCT* (pink) cell lines over the top 20% of CHD1 occupied genes (determined from a wild-type ChIP-seq dataset [22], $n = 4{,}101$). Data are averaged from three wild-type biological replicates and four *chd1ΔCHCT* replicates (two independent clones assayed in technical duplicate). The gray signal represents mononucleosome data from MNase-seq in mES cells [141]. Left *y*-axis: Relative CHD1 CUT&RUN enrichment. Right *y*-axis: Mononucleosome enrichment. (**C**) IGV browser tracks of CHD1 and H3K4me3 CUT&RUN data in indicated cell lines over *Nanog*. Data are averaged from 3–4 replicates. Information on replicates can be found in the Supplementary data file. (**D**) Metaplot of H3K4me3 CUT&RUN in wild-type (black), *chd1ΔCHCT* (pink), *chd2ΔCHCT* (orange), and *rtf1(AAAA)* (blue) cell lines as in panel (B). Data are averaged from three wild-type, *rtf1(AAAA)*, and *chd2ΔCHCT* biological replicates and four *chd1ΔCHCT* replicates [as in panel (B)]. (**E**) Mononucleosome (180–247 bp) ATAC-seq data at genes as in panel (B). Left *y*-axis: ATAC-seq enrichment. Right *y*-axis: Mononucleosome enrichment as in panel (B). Data are averaged from three wild-type, *rtf1(AAAA)*, and *chd2ΔCHCT* biological replicates and four *chd1ΔCHCT* replicates [as in panel (B)]. Information on replicates is provided in the Supplementary data file. (**F**) Mononucleosome (180–247 bp) ATAC-seq data over wild-type nucleosomes from top occupied CHD1 genes called using nucleoATAC [116]. The gray signal represents mononucleosome data from MNase-seq in wild-type mES cells. (**G**) ATAC-seq accessible footprints (1–100 bp) as in panel (E).

To test whether nucleosome positions are altered in the *chd1ΔCHCT*, *chd2ΔCHCT*, and *rtf1(AAAA)* cell lines relative to wild type, we performed CUT&RUN for H3K4me3 and H3K36me3. Visual examination of the spike-in normalized H3K4me3 CUT&RUN data demonstrate high resolution nucleosome positions with no visible shift or reduction in occupancy at either the top quintile of CHD1-occupied genes or over all genes (Fig. 6C and D and Supplementary Fig. S8A and B). Similarly, we did not observe a shift in H3K36me3 localization over gene bodies (Supplementary Fig. S8C and D). Total levels of H3, H3K4me3, and H3K36me3 are unchanged in these cell lines (Supplementary Fig. S8E).

While we did not see a change in position, we did observe a reproducible increase in H3K4me3 occupancy in the mutant cell lines (Fig. 6C and D and Supplementary Fig. S8A and B). Therefore, we individually depleted CHD1 and CHD2 in mES cells and performed H3K4me3 CUT&RUN (Supplementary Fig. S9A–D). These experiments showed a modest increase in H3K4me3 upon depletion of either CHD1 or CHD2, suggesting that the change in H3K4me3 occupancy arises from the hypomorphic nature of the mutant cell lines.

We next performed ATAC-seq to assess nucleosome positions. The nucleosome-size ATAC-seq reads also show no shift in nucleosome localization in the *rtf1(AAAA)*, *chd1ΔCHCT*, and *chd2ΔCHCT* cell lines relative to wild type, although this may be due to poor nucleosome footprinting beyond the +2 nucleosome (Fig. 6E and Supplementary Fig. S9E). We then called nucleosome peaks from wild-type ATAC-seq data using nucleoATAC over the top quintile of CHD1-occupied genes or over all genes and assessed the mononucleosome enrichment in all cell lines (Fig. 6F and Supplementary Fig. S9F) [116]. This analysis revealed no global shift in genic nucleosomes in the mutant cell lines. The accessible footprint from these ATAC-seq datasets shows a modest reduction in accessibility over promoters in all three cell lines relative to wild type, with *chd1ΔCHCT* showing the most prominent reduction (Fig. 6G and Supplementary Fig. S9G). These data suggest that while the interaction between RTF1 and CHD1/2 appears conserved, the chromatin structure over gene bodies in ES cells is robust to changes when only a single protein is mutated, likely due to many proteins contributing to nucleosome occupancy and positioning.

Discussion

In this study, we investigated the mechanistic basis of Chd1 localization to active genes during transcription elongation. We describe a direct interaction between the Paf1C subunit Rtf1 and Chd1, mediated by conserved regions that have been largely uncharacterized. Disruption of this interaction broadly affects Chd1 localization, causes a 5′ directional shift of mononucleosomes and other nucleosome species, and alters histone modification patterns in yeast. Our finding that homologous regions in mouse RTF1 and CHD1/2 can interact suggests that mammals and yeast may employ similar mechanisms for coupling nucleosome remodeling to transcription elongation.

Our previous work identified an interaction between yeast Rtf1 and Chd1, demonstrating that Chd1 functions on transcribed genes and is targeted there through interactions with the RNA Pol II elongation complex [19, 76]. Here, we report a direct interaction between these two proteins and show that a 30-amino acid region of Rtf1 and the CHCT domain of Chd1 are sufficient for this interaction. Despite a wealth of information on Chd1, very little is known about the functions of the CHCT domain. Most biochemical studies on purified Chd1 have omitted this domain, likely for technical reasons, and structural studies have yet to resolve the structure of the CHCT domain in the context of full-length Chd1 or a nucleosome substrate (e.g. [32], [34], [35], [40], and [41]). One study on the isolated human CHCT domain revealed a helical bundle fold comprised of five alpha helices by NMR and demonstrated dsDNA and nucleosome-binding activity *in vitro* [33]. Further, a yeast Chd1 construct lacking the CHCT domain remodels nucleosomes ∼1.5 times faster than full length Chd1 *in vitro*, suggesting an autoinhibitory role for the CHCT domain [33]. Interestingly, some of the conserved residues required for dsDNA binding by the human CHCT domain lie on alpha helix 5, which is predicted in yChd1 and mCHD1 to interface with yRtf1/mRTF1 (Fig. 1E and Supplementary Fig. S6G). Our data demonstrate that the CHCT domain is important for appropriate localization of Chd1 across gene bodies. Given the positioning of Rtf1 within the RNA Pol II elongation complex, it is possible that Rtf1 and DNA compete for binding to the CHCT domain and engage in a handoff mechanism through which nucleosome remodeling is temporally coordinated with transcription elongation. It will be interesting to determine how the dsDNA-binding and Rtf1-interacting functions of the CHCT domain contribute to overall Chd1 function.

The altered distribution of Chd1 in Rtf1–Chd1 interaction mutants is reflected in a 5′ shift in the distribution of different nucleosome species, as defined by the sizes of DNA fragments protected from MNase digestion. Mononucleosome positions in Rtf1 N-terminal and Chd1ΔCHCT mutants shift similarly at the +2, +3, and +4 nucleosomes. Beyond the +4 nucleosome, positioning is severely impacted such that nucleosome positions could not be reliably identified. The more modest change in mononucleosome positions in the *chd1Δ* strain agrees with results from previous MNase-seq studies [3, 5]. Reflecting the nucleosome shifts quantified using MNase-seq, genic H3K4me3 and H3K36me3 distributions determined by ChIP-seq are also impacted in Rtf1–Chd1 interaction mutants. Consistent with Chd1 and Isw1 having overlapping functions, we observed enhanced nucleosome positioning defects upon introducing the *isw1Δ* mutation into Rtf1–Chd1 interaction mutants. Together, these data reflect the importance of Chd1 in properly spacing nucleosomes such that when Chd1 localization is disrupted, nucleosome positions are shifted in the 5′ direction across gene bodies.

Changes in subnucleosome positions mirror the changes observed with mononucleosomes in the Rtf1–Chd1 interaction mutants. These subnucleosomes may be hexasomes, although further studies are necessary to define their precise composition. Hexasomes lacking distal H2A/H2B dimers are produced at the +1 position in mammals as a consequence of transcription elongation [127], and Chd1 is able to slide hexasomes when the H2A/H2B dimer is on the entry side of the substrate [128]. Interestingly, similar to our results with *chd1* mutants, deletion of *INO80*, which encodes the ATPase subunit of the Ino80 nucleosome remodeler complex, also results in a 5′ shift in the positions of mononucleosomes and subnucleosome particles [129].

The hexasome–nucleosome complex consists of a nucleosome that directly abuts a hexasome and has been increasingly studied in recent years [51, 124, 130, 131]. Chd1 binds

hexasome–nucleosome complexes and, following the FACT-mediated deposition of an H2A/H2B dimer to restore the nucleosome, remodels the new nucleosome to increase the distance between the two nucleosomes [51]. We observe a 5′ shift of hexasome–nucleosome complexes in our Rtf1–Chd1 interaction mutants. Dinucleosome-sized fragments, corresponding to tightly packed nucleosomes, were previously reported to accumulate in *chd1*Δ *isw1*Δ double mutants [13]. Our data show that disruption of the Rtf1–Chd1 interaction is sufficient to increase the relative levels of dinucleosomes, especially at the first and second positions, and shift their positioning 5′. Together with our analysis of mononucleosomes and sub-nucleosome particles, these changes in hexasome–nucleosome complexes and dinucleosomes indicate a broad role for Chd1 in resolving nucleosome species across actively transcribed genes. These molecular changes are reflected in the role of Chd1 in suppressing cryptic transcription [9].

The Rtf1–Chd1 interaction mutants exhibit stronger phenotypes than an *rtf1*Δ strain in several of our assays. The positions of mononucleosomes and other nucleosome species are less severely affected by the full deletion of *RTF1* than by specific mutations that disrupt the Rtf1–Chd1 interaction, although we observe poorly phased nucleosomes beyond the +4 position in both cases. ChIP-seq analysis also revealed a less pronounced shift in H3K36me3 distribution in the *rtf1*Δ strain compared to the *rtf1* point mutants. The *rtf1*Δ strain reflects the combined outcome of eliminating all Rtf1 functions, including interacting with Chd1, coupling Paf1C to Spt5, and promoting H2B ubiquitylation and downstream modifications such as H3K4me3 [61, 63, 64, 72, 74, 132, 133]. These functions likely act coordinately or even in opposition. Interestingly, the loss of some or all these functions might contribute to a redistribution of Chd1 such that more genes are occupied by Chd1 in *rtf1*Δ strains relative to wild type, where Chd1 is preferentially enriched at highly transcribed genes (Supplementary Fig. S3B). Collectively, our results highlight the importance of using specific point and domain mutations to understand the roles of proteins that have multiple functions and interacting partners.

The essential histone chaperone FACT is distributed across gene bodies in a manner dependent on Chd1 ATPase activity [17]. FACT binds to partially unwrapped H2A/H2B dimers and functions in a transcription-dependent manner [118, 134, 135]. FACT, Chd1, and Paf1C interact in yeast and mammals [19, 49, 50, 136]. While modest, Spt16 accumulates at the 5′ ends of genes in *rtf1*Δ cells, suggesting that the 5′ accumulation of Chd1 we observe in *rtf1*Δ may subsequently impact FACT distribution [17].

Through Y2H assays, we found that the interaction between mRTF1–mCHD1 and mRTF1–mCHD2 is conserved and occurs in a mRTF1 LLSLA box-dependent manner. Structure predictions indicate that several conserved leucine residues in yeast Rtf1, including the L4 position mutated for *in vivo* crosslinking and the L8 and L11 positions mutated for our functional studies, face a helix in the Chd1 CHCT. Mutation of analogous mRTF1 residues or deletion of the mCHD1/2 CHCT domain resulted in a loss of interaction by Y2H. Therefore, we hypothesized that mRTF1 LLSLA mutations and mCHD1/2 CHCT deletions would disrupt the predicted interaction in mES cells and shift nucleosome positioning and H3K4me3 and H3K36me3 patterns, as observed in yeast. We were surprised to observe that H3K4me3 and H3K36me3 localization, assessed by CUT&RUN, and mononucleosome positions, assessed by ATAC-seq, remained unchanged in RTF1(AAAA), CHD1ΔCHCT, and CHD2ΔCHCT cell lines relative to wild type. Given the large number of nucleosome remodelers in mammals, the mRTF1-CHCT interaction mutations may be insufficient to yield effects at the chromatin level. It may also be that the mRTF1–mCHD1/2 interactions involve sequences outside of the minimally interacting regions such that our specific mutations are insufficient to disrupt these interactions. This possibility is supported by our Y2H results using longer constructs (Fig. 5E). Alternatively, for mCHD1, the chromodomain-H3K4me3 interaction may be a stronger driver of CHD1 targeting with the RTF1–CHD1 interaction playing a modulatory role [43, 44]. However, using the analog H3K4Cme3, a recent study found that this modification does not change the nucleosome sliding rate of human CHD1 and confers only a modest increase in affinity of CHD1 for nucleosomes [40]. Therefore, it remains possible that the mRTF1–mCHD1 and mRTF1–mCHD2 interactions detected in our study support an H3K4me3-independent mechanism for CHD1 recruitment and a potential pathway through which mCHD2, which has weak affinity for H3K4me3, is targeted to gene bodies [45].

Previous studies using prostate cancer cell lines depleted of hCHD1 or mouse embryonic fibroblasts overexpressing a dominant negative version of mCHD1 reported a reduction in H3K4me3 occupancy and nucleosome occupancy, respectively [137, 138]. However, we did not observe a reduction in H3K4me3 in either the CHD1ΔCHCT cell line or upon depletion of CHD1 and instead observed a modest increase in spike-in normalized H3K4me3 CUT&RUN experiments, despite reduced abundance of mCHD1. These differences may be cell line specific, due to different protein levels, and/or reflect the need for spike-in normalization.

In summary, our study shows that a direct interaction between Rtf1 and Chd1 is required for the distribution of Chd1 across transcribed genes in yeast and, as a consequence, the proper distribution of nucleosomes and associated histone modifications. These results demonstrate the necessity for Chd1 and its coupling to the RNA Pol II elongation complex in the re-establishment of chromatin structure in the wake of RNA Pol II. Specifically, our data argue that a functional Chd1-Rtf1 interaction is required to shift all nucleosome species in the 3′ direction, counteracting the retrograde movement of nucleosomes caused by RNA Pol II passage [139]. Further investigation into the conservation of this interaction and its function amid overlapping chromatin regulatory inputs may provide additional insights into the significance of the RTF1-CHCT interaction in mammalian cells.

Acknowledgements

We are grateful to Alex Lederer, Sanhita Kutumbaka, and Matthew Hurton for technical assistance, Craig Kaplan and Fred Winston for providing yeast strains and plasmids, Jeff Brodsky for Sse1 antisera, Greg Bowman for communicating updated information on Chd1 domain boundaries, and members of the Arndt lab, especially Alex Francette, Aakash Grover, and Mitch Ellison, and the Hainer lab for helpful discussions. Molecular graphics and analyses were performed with UCSF ChimeraX, developed by the Resource for Biocomputing, Visualization, and Informatics at the University of California, San Francisco, with support from National Institutes

of Health R01-GM129325 and the Office of Cyber Infrastructure and Computational Biology, National Institute of Allergy and Infectious Diseases. This research was supported in part by the University of Pittsburgh Center for Research Computing, RRID:SCR_022735, through the resources provided. Specifically, this work used the HTC cluster, which is supported by NIH award number S10OD028483. This project used the University of Pittsburgh HSCRF Genomics Research Core, RRID: SCR_018301 NGS sequencing services, with special thanks to the Assistant Director, Will MacDonald.

Author contributions: Sarah A. Tripplehorn (Conceptualization [supporting], Data curation [supporting], Formal analysis [supporting], Funding acquisition [supporting], Investigation [equal], Methodology [equal], Visualization [equal], Writing—original draft [equal]), Santana M. Lardo (Data curation [supporting], Investigation [equal], Methodology [equal], Visualization [equal], Writing—original draft [supporting], Writing—review & editing [supporting]), Margaret K. Shirra (Conceptualization [supporting], Data curation [supporting], Investigation [supporting], Methodology [supporting], Visualization [supporting], Writing—original draft [supporting], Writing—review & editing [supporting]), Hannah G. Marvil (Data curation [supporting], Investigation [supporting], Methodology [supporting], Validation [supporting], Writing—review & editing [supporting]), Sarah Jane Hainer (Conceptualization [equal], Data curation [supporting], Formal analysis [lead], Funding acquisition [equal], Project administration [equal], Supervision [equal], Validation [equal], Visualization [supporting], Writing—original draft [equal], Writing—review & editing [equal]), Karen M. Arndt (Conceptualization [equal], Funding acquisition [equal], Project administration [equal], Supervision [equal], Validation [equal], Writing—original draft [lead], Writing—review & editing [equal])

Supplementary data

Supplementary data are available at NAR online.

Conflict of interest

None declared.

Funding

This work was supported by the National Institutes of Health [R35 GM141964 to K.M.A., T32 GM133353 to S.A.T., and R35 GM133732 to S.J.H.]. This work is open access as per the NIH Public Access Policy, with PMC accessibility.

Data availability

ChIP-seq, MNase-seq, CUT&RUN, and ATAC-seq data have been deposited at the Gene Expression Omnibus and are publicly available. Accession numbers are: GSE280670 (ChIP-seq); GSE280671 (MNase-seq); GSE281937 (CUT&RUN); and GSE282106 (ATAC-seq). All other data supporting the key findings are available in the article and supplementary materials.

References

1. Clapier CR, Iwasa J, Cairns BR *et al.* Mechanisms of action and regulation of ATP-dependent chromatin-remodelling complexes. *Genes Dev.* 2017;**18**:362–78. https://doi.org/10.1038/nrm.2017.26
2. Gourisankar S, Krokhotin A, Wenderski W *et al.* Context-specific functions of chromatin remodellers in development and disease. *Nat. Rev. Genet.* 2024;**25**:340–61. https://doi.org/10.1038/s41576-023-00666-x
3. Gkikopoulos T, Schofield P, Singh V *et al.* A role for Snf2-related nucleosome-spacing enzymes in genome-wide nucleosome organization. *Science* 2011;**333**:1758–60. https://doi.org/10.1126/science.1206097
4. Hughes AL, Rando OJ. Comparative genomics reveals Chd1 as a determinant of nucleosome spacing *in vivo*. *G3 (Bethesda)* 2015;**5**:1889–97. https://doi.org/10.1534/g3.115.020271
5. Ocampo J, Chereji RV, Eriksson PR *et al.* . The ISW1 and CHD1 ATP-dependent chromatin remodelers compete to set nucleosome spacing *in vivo*. *Nucleic Acids Res.* 2016;**44**:4625–35. https://doi.org/10.1093/nar/gkw068
6. Ocampo J, Chereji RV, Eriksson PR *et al.* Contrasting roles of the RSC and ISW1/CHD1 chromatin remodelers in RNA polymerase II elongation and termination. *Genome Res.* 2019;**29**:407–17. https://doi.org/10.1101/gr.242032.118
7. Tran HG, Steger DJ, Iyer VR *et al.* The chromo domain protein Chd1p from budding yeast is an ATP-dependent chromatin-modifying factor. *EMBO J.* 2000;**19**:2323–31. https://doi.org/10.1093/emboj/19.10.2323
8. Vary JC Jr, Gangaraju VK, Qin J *et al.* Yeast Isw1p forms two separable complexes *in vivo*. *Mol. Cell. Biol.* 2003;**23**:80–91. https://doi.org/10.1128/MCB.23.1.80-91.2003
9. Cheung V, Chua G, Batada NN *et al.* Chromatin- and transcription-related factors repress transcription from within coding regions throughout the *Saccharomyces cerevisiae* genome. *PLoS Biol.* 2008;**6**:e277. https://doi.org/10.1371/journal.pbio.0060277
10. Lee Y, Park D, Iyer VR. The ATP-dependent chromatin remodeler Chd1 is recruited by transcription elongation factors and maintains H3K4me3/H3K36me3 domains at actively transcribed and spliced genes. *Nucleic Acids Res.* 2017;**45**:7180–90. https://doi.org/10.1093/nar/gkx321
11. Radman-Livaja M, Quan TK, Valenzuela L *et al.* A key role for Chd1 in histone H3 dynamics at the 3′ ends of long genes in yeast. *PLoS Genet.* 2012;**8**:e1002811. https://doi.org/10.1371/journal.pgen.1002811
12. Smolle M, Venkatesh S, Gogol MM *et al.* Chromatin remodelers Isw1 and Chd1 maintain chromatin structure during transcription by preventing histone exchange. *Nat. Struct. Mol. Biol.* 2012;**19**:884–92. https://doi.org/10.1038/nsmb.2312
13. Eriksson PR, Clark DJ. The yeast ISW1b ATP-dependent chromatin remodeler is critical for nucleosome spacing and dinucleosome resolution. *Sci. Rep.* 2021;**11**:4195. https://doi.org/10.1038/s41598-021-82842-9
14. Konev AY, Tribus M, Park SY *et al.* CHD1 motor protein is required for deposition of histone variant H3.3 into chromatin *in vivo*. *Science* 2007;**317**:1087–90. https://doi.org/10.1126/science.1145339
15. Lusser A, Urwin DL, Kadonaga JT. Distinct activities of CHD1 and ACF in ATP-dependent chromatin assembly. *Nat. Struct. Mol. Biol.* 2005;**12**:160–6. https://doi.org/10.1038/nsmb884
16. Torigoe SE, Patel A, Khuong MT *et al.* ATP-dependent chromatin assembly is functionally distinct from chromatin remodeling. *eLife* 2013;**2**:e00863. https://doi.org/10.7554/eLife.00863
17. Jeronimo C, Angel A, Nguyen VQ *et al.* FACT is recruited to the +1 nucleosome of transcribed genes and spreads in a Chd1-dependent manner. *Mol. Cell* 2021;**81**:3542–59. https://doi.org/10.1016/j.molcel.2021.07.010
18. Park D, Shivram H, Iyer VR. Chd1 co-localizes with early transcription elongation factors independently of H3K36

methylation and releases stalled RNA polymerase II at introns. *Epigenetics Chromatin* 2014;**7**:32. https://doi.org/10.1186/1756-8935-7-32
19. Simic R, Lindstrom DL, Tran HG *et al.* Chromatin remodeling protein Chd1 interacts with transcription elongation factors and localizes to transcribed genes. *EMBO J.* 2003;**22**:1846–56. https://doi.org/10.1093/emboj/cdg179
20. Trujillo JT, Long J, Aboelnour E *et al.* CHD chromatin remodeling protein diversification yields novel clades and domains absent in classic model organisms. *Genome Biol. Evol.* 2022;**14**: evac066. https://doi.org/10.1093/gbe/evac066
21. Siggens L, Cordeddu L, Ronnerblad M *et al.* Transcription-coupled recruitment of human CHD1 and CHD2 influences chromatin accessibility and histone H3 and H3.3 occupancy at active chromatin regions. *Epigenetics Chromatin* 2015;**8**:4. https://doi.org/10.1186/1756-8935-8-4
22. de Dieuleveult M, Yen K, Hmitou I *et al.* Genome-wide nucleosome specificity and function of chromatin remodellers in ES cells. *Nature* 2016;**530**:113–6. https://doi.org/10.1038/nature16505
23. Gaspar-Maia A, Alajem A, Polesso F *et al.* Chd1 regulates open chromatin and pluripotency of embryonic stem cells. *Nature* 2009;**460**:863–8. https://doi.org/10.1038/nature08212
24. Guzman-Ayala M, Sachs M, Koh FM *et al.* Chd1 is essential for the high transcriptional output and rapid growth of the mouse epiblast. *Development* 2015;**142**:118–27. https://doi.org/10.1242/dev.114843
25. Kim YJ, Khoshkhoo S, Frankowski JC *et al.* Chd2 is necessary for neural circuit development and long-term memory. *Neuron* 2018;**100**:1180–93. https://doi.org/10.1016/j.neuron.2018.09.049
26. Shen T, Ji F, Yuan Z *et al.* CHD2 is required for embryonic neurogenesis in the developing cerebral cortex. *Stem Cells* 2015;**33**:1794–806. https://doi.org/10.1002/stem.2001
27. Marfella CG, Ohkawa Y, Coles AH *et al.* Mutation of the SNF2 family member Chd2 affects mouse development and survival. *J. Cell. Physiol.* 2006;**209**:162–71. https://doi.org/10.1002/jcp.20718
28. Nodelman IM, Bowman GD. Biophysics of chromatin remodeling. *Annu. Rev. Biophys.* 2021;**50**:73–93. https://doi.org/10.1146/annurev-biophys-082520-080201
29. Nodelman IM, Shen Z, Levendosky RF *et al.* Autoinhibitory elements of the Chd1 remodeler block initiation of twist defects by destabilizing the ATPase motor on the nucleosome. *Proc. Natl. Acad. Sci. USA* 2021;**118**:e2014498118. https://doi.org/10.1073/pnas.2014498118
30. Winger J, Nodelman IM, Levendosky RF *et al.* A twist defect mechanism for ATP-dependent translocation of nucleosomal DNA. *eLife* 2018;**7**:e34100. https://doi.org/10.7554/eLife.34100
31. Delmas V, Stokes DG, Perry RP. A mammalian DNA-binding protein that contains a chromodomain and an SNF2/SWI2-like helicase domain. *Proc. Natl. Acad. Sci. USA* 1993;**90**:2414–8. https://doi.org/10.1073/pnas.90.6.2414
32. Farnung L, Vos SM, Wigge C *et al.* Nucleosome-Chd1 structure and implications for chromatin remodelling. *Nature* 2017;**550**:539–42. https://doi.org/10.1038/nature24046
33. Mohanty B, Helder S, Silva AP *et al.* The chromatin remodelling protein CHD1 contains a previously unrecognised C-terminal helical domain. *J. Mol. Biol.* 2016;**428**:4298–314. https://doi.org/10.1016/j.jmb.2016.08.028
34. Nodelman IM, Das S, Faustino AM *et al.* Nucleosome recognition and DNA distortion by the Chd1 remodeler in a nucleotide-free state. *Nat. Struct. Mol. Biol.* 2022;**29**:121–9. https://doi.org/10.1038/s41594-021-00719-x
35. Hauk G, McKnight JN, Nodelman IM *et al.* The chromodomains of the Chd1 chromatin remodeler regulate DNA access to the ATPase motor. *Mol. Cell* 2010;**39**:711–23. https://doi.org/10.1016/j.molcel.2010.08.012
36. McKnight JN, Jenkins KR, Nodelman IM *et al.* Extranucleosomal DNA binding directs nucleosome sliding by Chd1. *Mol. Cell. Biol.* 2011;**31**:4746–59. https://doi.org/10.1128/MCB.05735-11
37. Ryan DP, Sundaramoorthy R, Martin D *et al.* The DNA-binding domain of the Chd1 chromatin-remodelling enzyme contains SANT and SLIDE domains. *EMBO J.* 2011;**30**:2596–609. https://doi.org/10.1038/emboj.2011.166
38. Sharma A, Jenkins KR, Heroux A *et al.* Crystal structure of the chromodomain helicase DNA-binding protein 1 (Chd1) DNA-binding domain in complex with DNA. *J. Biol. Chem.* 2011;**286**:42099–104. https://doi.org/10.1074/jbc.C111.294462
39. Stokes DG, Perry RP. DNA-binding and chromatin localization properties of CHD1. *Mol. Cell. Biol.* 1995;**15**:2745–53. https://doi.org/10.1128/MCB.15.5.2745
40. James AM, Farnung L. Structural basis of human CHD1 nucleosome recruitment and pausing. *Mol. Cell* 2025;**85**:1938–51. https://doi.org/10.1016/j.molcel.2025.04.020
41. Nodelman IM, Folkwein HJ, Glime WS *et al.* A competitive regulatory mechanism of the Chd1 remodeler is integral to distorting nucleosomal DNA. *Nat. Struct. Mol. Biol.* 2025; **32**:1445–55. https://doi.org/10.1038/s41594-025-01556-y
42. Bartke T, Vermeulen M, Xhemalce B *et al.* Nucleosome-interacting proteins regulated by DNA and histone methylation. *Cell* 2010;**143**:470–84. https://doi.org/10.1016/j.cell.2010.10.012
43. Flanagan JF, Mi LZ, Chruszcz M *et al.* Double chromodomains cooperate to recognize the methylated histone H3 tail. *Nature* 2005;**438**:1181–5. https://doi.org/10.1038/nature04290
44. Sims RJ 3rd, Chen CF, Santos-Rosa H *et al.* Human but not yeast CHD1 binds directly and selectively to histone H3 methylated at lysine 4 via its tandem chromodomains. *J. Biol. Chem.* 2005;**280**:41789–92. https://doi.org/10.1074/jbc.C500395200
45. Flanagan JF, Blus BJ, Kim D *et al.* Molecular implications of evolutionary differences in CHD double chromodomains. *J. Mol. Biol.* 2007;**369**:334–42. https://doi.org/10.1016/j.jmb.2007.03.024
46. Okuda M, Horikoshi M, Nishimura Y. Structural polymorphism of chromodomains in Chd1. *J. Mol. Biol.* 2007;**365**:1047–62. https://doi.org/10.1016/j.jmb.2006.10.039
47. Santos-Rosa H, Schneider R, Bernstein BE *et al.* Methylation of histone H3 K4 mediates association of the Isw1p ATPase with chromatin. *Mol. Cell* 2003;**12**:1325–32. https://doi.org/10.1016/S1097-2765(03)00438-6
48. Morettini S, Tribus M, Zeilner A *et al.* The chromodomains of CHD1 are critical for enzymatic activity but less important for chromatin localization. *Nucleic Acids Res.* 2011;**39**:3103–15. https://doi.org/10.1093/nar/gkq1298
49. Kelley DE, Stokes DG, Perry RP. CHD1 interacts with SSRP1 and depends on both its chromodomain and its ATPase/helicase-like domain for proper association with chromatin. *Chromosoma* 1999;**108**:10–25. https://doi.org/10.1007/s004120050347
50. Krogan NJ, Kim M, Ahn SH *et al.* RNA polymerase II elongation factors of *Saccharomyces cerevisiae*: a targeted proteomics approach. *Mol. Cell. Biol.* 2002;**22**:6979–92. https://doi.org/10.1128/MCB.22.20.6979-6992.2002
51. Engeholm M, Roske JJ, Oberbeckmann E *et al.* Resolution of transcription-induced hexasome–nucleosome complexes by Chd1 and FACT. *Mol. Cell* 2024;**84**:3423–37. https://doi.org/10.1016/j.molcel.2024.08.022
52. Squazzo SL, Costa PJ, Lindstrom DL *et al.* The Paf1 complex physically and functionally associates with transcription elongation factors *in vivo*. *EMBO J.* 2002;**21**:1764–74. https://doi.org/10.1093/emboj/21.7.1764
53. Vos SM, Farnung L, Linden A *et al.* Structure of complete Pol II-DSIF-PAF-SPT6 transcription complex reveals RTF1 allosteric activation. *Nat. Struct. Mol. Biol.* 2020;**27**:668–77. https://doi.org/10.1038/s41594-020-0437-1
54. Francette AM, Arndt KM. Multiple direct and indirect roles of the Paf1 complex in transcription elongation, splicing, and

histone modifications. *Cell Rep*. 2024;**43**:114730. https://doi.org/10.1016/j.celrep.2024.114730
55. Hou L, Wang Y, Liu Y *et al*. Paf1C regulates RNA polymerase II progression by modulating elongation rate. *Proc. Natl. Acad. Sci. USA* 2019;**116**:14583–92. https://doi.org/10.1073/pnas.1904324116
56. Santana JF, Spector BM, Suarez GA *et al*. NELF focuses sites of initiation and maintains promoter architecture. *Nucleic Acids Res*. 2024;**52**:2977–94. https://doi.org/10.1093/nar/gkad1253
57. Zumer K, Maier KC, Farnung L *et al*. Two distinct mechanisms of RNA polymerase II elongation stimulation *in vivo*. *Mol. Cell* 2021;**81**:3096–109. https://doi.org/10.1016/j.molcel.2021.05.028
58. Fetian T, McShane BM, Horan NL *et al*. Paf1 complex subunit Rtf1 stimulates H2B ubiquitylation by interacting with the highly conserved N-terminal helix of Rad6. *Proc. Natl. Acad. Sci. USA* 2023;**120**:e2220041120. https://doi.org/10.1073/pnas.2220041120
59. Kim J, Guermah M, McGinty RK *et al*. RAD6-Mediated transcription-coupled H2B ubiquitylation directly stimulates H3K4 methylation in human cells. *Cell* 2009;**137**:459–71. https://doi.org/10.1016/j.cell.2009.02.027
60. Krogan NJ, Dover J, Wood A *et al*. The Paf1 complex is required for histone H3 methylation by COMPASS and Dot1p: linking transcriptional elongation to histone methylation. *Mol. Cell* 2003;**11**:721–9. https://doi.org/10.1016/S1097-2765(03)00091-1
61. Ng HH, Dole S, Struhl K. The Rtf1 component of the Paf1 transcriptional elongation complex is required for ubiquitination of histone H2B. *J. Biol. Chem*. 2003;**278**:33625–8. https://doi.org/10.1074/jbc.C300270200
62. Ng HH, Robert F, Young RA *et al*. Targeted recruitment of Set1 histone methylase by elongating Pol II provides a localized mark and memory of recent transcriptional activity. *Mol. Cell* 2003;**11**:709–19. https://doi.org/10.1016/S1097-2765(03)00092-3
63. Van Oss SB, Shirra MK, Bataille AR *et al*. The histone modification domain of Paf1 complex subunit Rtf1 directly stimulates H2B ubiquitylation through an interaction with Rad6. *Mol. Cell* 2016;**64**:815–25. https://doi.org/10.1016/j.molcel.2016.10.008
64. Wood A, Schneider J, Dover J *et al*. The Paf1 complex is essential for histone monoubiquitination by the Rad6-Bre1 complex, which signals for histone methylation by COMPASS and Dot1p. *J. Biol. Chem*. 2003;**278**:34739–42. https://doi.org/10.1074/jbc.C300269200
65. Sheldon KE, Mauger DM, Arndt KM. A requirement for the *Saccharomyces cerevisiae* Paf1 complex in snoRNA 3′ end formation. *Mol. Cell* 2005;**20**:225–36. https://doi.org/10.1016/j.molcel.2005.08.026
66. Yang Y, Li W, Hoque M *et al*. PAF complex plays novel subunit-specific roles in alternative cleavage and polyadenylation. *PLoS Genet*. 2016;**12**:e1005794. https://doi.org/10.1371/journal.pgen.1005794
67. Chen FX, Woodfin AR, Gardini A *et al*. PAF1, a molecular regulator of promoter-proximal pausing by RNA polymerase II. *Cell* 2015;**162**:1003–15. https://doi.org/10.1016/j.cell.2015.07.042
68. Yu M, Yang W, Ni T *et al*. RNA polymerase II-associated factor 1 regulates the release and phosphorylation of paused RNA polymerase II. *Science* 2015;**350**:1383–6. https://doi.org/10.1126/science.aad2338
69. Mueller CL, Jaehning JA. Ctr9, Rtf1, and Leo1 are components of the Paf1/RNA polymerase II complex. *Mol. Cell. Biol*. 2002;**22**:1971–80. https://doi.org/10.1128/MCB.22.7.1971-1980.2002
70. Zhu B, Mandal SS, Pham AD *et al*. The human PAF complex coordinates transcription with events downstream of RNA synthesis. *Genes Dev*. 2005;**19**:1668–73. https://doi.org/10.1101/gad.1292105
71. Ellison MA, Namjilsuren S, Shirra MK *et al*. Spt6 directly interacts with Cdc73 and is required for Paf1 complex occupancy at active genes in *Saccharomyces cerevisiae*. *Nucleic Acids Res*. 2023;**51**:4814–30. https://doi.org/10.1093/nar/gkad180
72. Mayekar MK, Gardner RG, Arndt KM. The recruitment of the *Saccharomyces cerevisiae* Paf1 complex to active genes requires a domain of Rtf1 that directly interacts with the Spt4–Spt5 complex. *Mol. Cell. Biol*. 2013;**33**:3259–73. https://doi.org/10.1128/MCB.00270-13
73. Vos SM, Farnung L, Boehning M *et al*. Structure of activated transcription complex Pol II-DSIF-PAF-SPT6. *Nature* 2018;**560**:607–12. https://doi.org/10.1038/s41586-018-0440-4
74. Wier AD, Mayekar MK, Heroux A *et al*. Structural basis for Spt5-mediated recruitment of the Paf1 complex to chromatin. *Proc. Natl. Acad. Sci. USA* 2013;**110**:17290–5. https://doi.org/10.1073/pnas.1314754110
75. Cao QF, Yamamoto J, Isobe T *et al*. Characterization of the human transcription elongation factor Rtf1: evidence for nonoverlapping functions of Rtf1 and the Paf1 complex. *Mol. Cell. Biol*. 2015;**35**:3459–70. https://doi.org/10.1128/MCB.00601-15
76. Warner MH, Roinick KL, Arndt KM. Rtf1 is a multifunctional component of the Paf1 complex that regulates gene expression by directing cotranscriptional histone modification. *Mol. Cell. Biol*. 2007;**27**:6103–15. https://doi.org/10.1128/MCB.00772-07
77. Kim S, Bugga L, Hong ES *et al*. An RNAi-based candidate screen for modifiers of the CHD1 chromatin remodeler and assembly factor in *Drosophila melanogaster*. *G3* 2015;**6**:245–54. https://doi.org/10.1534/g3.115.021691
78. Winston F, Dollard C, Ricupero-Hovasse SL. Construction of a set of convenient *Saccharomyces cerevisiae* strains that are isogenic to S288C. *Yeast* 1995;**11**:53–5. https://doi.org/10.1002/yea.320110107
79. James P, Halladay J, Craig EA. Genomic libraries and a host strain designed for highly efficient two-hybrid selection in yeast. *Genetics* 1996;**144**:1425–36. https://doi.org/10.1093/genetics/144.4.1425
80. Rose MD, Winston F, Hieter P. *Methods in Yeast Genetics: A Laboratory Course Manual*. Cold Spring Harbor Laboratory Press, Cold Spring Harbor, NY. 1990.
81. Storici F, Resnick MA. The *delitto perfetto* approach to *in vivo* site-directed mutagenesis and chromosome rearrangements with synthetic oligonucleotides in yeast. *Methods Enzymol*. 2006;**409**:329–45.
82. Funakoshi M, Hochstrasser M. Small epitope-linker modules for PCR-based C-terminal tagging in *Saccharomyces cerevisiae*. *Yeast* 2009;**26**:185–92. https://doi.org/10.1002/yea.1658
83. Rutherford KM, Lera-Ramirez M, Wood V. PomBase: a global core biodata resource-growth, collaboration, and sustainability. *Genetics* 2024;**227**:iyae007. https://doi.org/10.1093/genetics/iyae007
84. Bahler J, Wu JQ, Longtine MS *et al*. Heterologous modules for efficient and versatile PCR-based gene targeting in *Schizosaccharomyces pombe*. *Yeast* 1998;**14**:943–51. https://doi.org/10.1002/(SICI)1097-0061(199807)14:10%3c943::AID-YEA292%3e3.0.CO;2-Y
85. Doench JG, Fusi N, Sullender M *et al*. Optimized sgRNA design to maximize activity and minimize off-target effects of CRISPR-Cas9. *Nat. Biotechnol*. 2016;**34**:184–91. https://doi.org/10.1038/nbt.3437
86. Sanson KR, Hanna RE, Hegde M *et al*. Optimized libraries for CRISPR-Cas9 genetic screens with multiple modalities. *Nat. Commun*. 2018;**9**:5416. https://doi.org/10.1038/s41467-018-07901-8
87. Gutschner T, Haemmerle M, Genovese G *et al*. Post-translational regulation of Cas9 during G1 enhances homology-directed

repair. *Cell Rep*. 2016;**14**:1555–66. https://doi.org/10.1016/j.celrep.2016.01.019
88. Klein DC, Lardo SM, McCannell KN *et al.* FACT regulates pluripotency through proximal and distal regulation of gene expression in murine embryonic stem cells. *BMC Biol*. 2023;**21**:167. https://doi.org/10.1186/s12915-023-01669-0
89. Yang D, Buchholz F, Huang Z *et al.* Short RNA duplexes produced by hydrolysis with *Escherichia coli* RNase III mediate effective RNA interference in mammalian cells. *Proc. Natl. Acad. Sci. USA* 2002;**99**:9942–7. https://doi.org/10.1073/pnas.152327299
90. Stolinski LA, Eisenmann DM, Arndt KM. Identification of *RTF1*, a novel gene important for TATA site selection by TATA box-binding protein in *Saccharomyces cerevisiae*. *Mol. Cell. Biol*. 1997;**17**:4490–500. https://doi.org/10.1128/MCB.17.8.4490
91. Kunkel TA, Roberts JD, Zakour RA. Rapid and efficient site-specific mutagenesis without phenotypic selection. *Methods Enzymol*. 1987;**154**:367–82.
92. Bartel PL, Chien C-T, Sternglanz R *et al. Cellular Interactions in Development: A Practical Approach*. Oxford University Press, Oxford, United Kingdom, 1993;153–79. https://doi.org/10.1093/oso/9780199633913.001.0001
93. Sievers F, Wilm A, Dineen D *et al.* Fast, scalable generation of high-quality protein multiple sequence alignments using Clustal Omega. *Mol. Syst. Biol*. 2011;**7**:539. https://doi.org/10.1038/msb.2011.75
94. UniProt C. UniProt: 539 the universal protein knowledgebase in 2023. *Nucleic Acids Res*. 2023;**51**:D523–31.
95. Waterhouse AM, Procter JB, Martin DM *et al.* Jalview Version 2–a multiple sequence alignment editor and analysis workbench. *Bioinformatics* 2009;**25**:1189–91. https://doi.org/10.1093/bioinformatics/btp033
96. Cucinotta CE, Hildreth AE, McShane BM *et al.* The nucleosome acidic patch directly interacts with subunits of the Paf1 and FACT complexes and controls chromatin architecture *in vivo*. *Nucleic Acids Res*. 2019;**47**:8410–23. https://doi.org/10.1093/nar/gkz549
97. Abramson J, Adler J, Dunger J *et al.* Accurate structure prediction of biomolecular interactions with AlphaFold 3. *Nature* 2024;**630**:493–500. https://doi.org/10.1038/s41586-024-07487-w
98. Meng EC, Goddard TD, Pettersen EF *et al.* UCSF ChimeraX: tools for structure building and analysis. *Protein Sci*. 2023;**32**:e4792. https://doi.org/10.1002/pro.4792
99. Cucinotta CE, Young AN, Klucevsek KM *et al.* The nucleosome acidic patch regulates the H2B K123 monoubiquitylation cascade and transcription elongation in *Saccharomyces cerevisiae*. *PLoS Genet*. 2015;**11**:e1005420. https://doi.org/10.1371/journal.pgen.1005420
100. Doris SM, Chuang J, Viktorovskaya O *et al.* Spt6 is required for the fidelity of promoter selection. *Mol. Cell* 2018;**72**:687–99. https://doi.org/10.1016/j.molcel.2018.09.005
101. Kushnirov VV. Rapid and reliable protein extraction from yeast. *Yeast* 2000;**16**:857–60. https://doi.org/10.1002/1097-0061(20000630)16:9%3c857::AID-YEA561%3e3.0.CO;2-B
102. Hainer SJ, Boskovic A, McCannell KN *et al.* Profiling of pluripotency factors in single cells and early embryos. *Cell* 2019;**177**:1319–29. https://doi.org/10.1016/j.cell.2019.03.014
103. Hainer SJ, Fazzio TG. High-resolution chromatin profiling using CUT&RUN. *Curr. Protoc. Mol. Biol*. 2019;**126**:e85.
104. Patty BJ, Dhungana R, Hainer SJ. Widespread impact of nucleosome remodelers on transcription at cis-regulatory elements. *Cell Rep*. 2025;**44**:115767. https://doi.org/10.1016/j.celrep.2025.115767
105. Skene PJ, Henikoff S. An efficient targeted nuclease strategy for high-resolution mapping of DNA binding sites. *eLife* 2017;**6**:e21856. https://doi.org/10.7554/eLife.21856
106. Buenrostro JD, Giresi PG, Zaba LC *et al.* Transposition of native chromatin for fast and sensitive epigenomic profiling of open chromatin, DNA-binding proteins and nucleosome position. *Nat. Methods* 2013;**10**:1213–8. https://doi.org/10.1038/nmeth.2688
107. Bolger AM, Lohse M, Usadel B. Trimmomatic: a flexible trimmer for Illumina sequence data. *Bioinformatics* 2014;**30**:2114–20. https://doi.org/10.1093/bioinformatics/btu170
108. Langmead B, Salzberg SL. Fast gapped-read alignment with Bowtie 2. *Nat. Methods* 2012;**9**:357–9. https://doi.org/10.1038/nmeth.1923
109. Danecek P, Bonfield JK, Liddle J *et al.* . Twelve years of SAMtools and BCFtools. *Gigascience* 2021;**10**:giab008.
110. Jeronimo C, Poitras C, Robert F. Histone recycling by FACT and Spt6 during transcription prevents the scrambling of histone modifications. *Cell Rep*. 2019;**28**:1206–18. https://doi.org/10.1016/j.celrep.2019.06.097
111. Ramirez F, Ryan DP, Gruning B *et al.* deepTools2: a next generation web server for deep-sequencing data analysis. *Nucleic Acids Res*. 2016;**44**:W160–65. https://doi.org/10.1093/nar/gkw257
112. Zerbino DR, Johnson N, Juettemann T *et al.* WiggleTools: parallel processing of large collections of genome-wide datasets for visualization and statistical analysis. *Bioinformatics* 2014;**30**:1008–9. https://doi.org/10.1093/bioinformatics/btt737
113. Chereji RV, Ramachandran S, Bryson TD *et al.* Precise genome-wide mapping of single nucleosomes and linkers *in vivo*. *Genome Biol*. 2018;**19**:19. https://doi.org/10.1186/s13059-018-1398-0
114. Orlando DA, Chen MW, Brown VE *et al.* Quantitative ChIP-seq normalization reveals global modulation of the epigenome. *Cell Rep*. 2014;**9**:1163–70. https://doi.org/10.1016/j.celrep.2014.10.018
115. Smith JP, Corces MR, Xu J *et al.* PEPATAC: an optimized pipeline for ATAC-seq data analysis with serial alignments. *NAR Genom. Bioinform*. 2021;**3**:lqab101. https://doi.org/10.1093/nargab/lqab101
116. Schep AN, Buenrostro JD, Denny SK *et al.* Structured nucleosome fingerprints enable high-resolution mapping of chromatin architecture within regulatory regions. *Genome Res*. 2015;**25**:1757–70. https://doi.org/10.1101/gr.192294.115
117. Chin JW, Cropp TA, Anderson JC *et al.* An expanded eukaryotic genetic code. *Science* 2003;**301**:964–7. https://doi.org/10.1126/science.1084772
118. Ehara H, Kujirai T, Shirouzu M *et al.* Structural basis of nucleosome disassembly and reassembly by RNAPII elongation complex with FACT. *Science* 2022;**377**: eabp9466. https://doi.org/10.1126/science.abp9466
119. Markert JW, Soffers JH, Farnung L. Structural basis of H3K36 trimethylation by SETD2 during chromatin transcription. *Science* 2025;**387**:528–33. https://doi.org/10.1126/science.adn6319
120. Kaplan CD, Laprade L, Winston F. Transcription elongation factors repress transcription initiation from cryptic sites. *Science* 2003;**301**:1096–9. https://doi.org/10.1126/science.1087374
121. Krietenstein N, Wal M, Watanabe S *et al.* Genomic nucleosome organization reconstituted with pure proteins. *Cell* 2016;**167**:709–21. https://doi.org/10.1016/j.cell.2016.09.045
122. Pointner J, Persson J, Prasad P *et al.* CHD1 remodelers regulate nucleosome spacing *in vitro* and align nucleosomal arrays over gene coding regions in *S. pombe*. *EMBO J*. 2012;**31**:4388–403. https://doi.org/10.1038/emboj.2012.289
123. Tsukiyama T, Palmer J, Landel CC *et al.* Characterization of the imitation switch subfamily of ATP-dependent chromatin-remodeling factors in *Saccharomyces cerevisiae*. *Genes Dev*. 1999;**13**:686–97. https://doi.org/10.1101/gad.13.6.686
124. Engeholm M, de Jager M, Flaus A *et al.* Nucleosomes can invade DNA territories occupied by their neighbors. *Nat. Struct. Mol. Biol*. 2009;**16**:151–8. https://doi.org/10.1038/nsmb.1551
125. Millan-Zambrano G, Burton A, Bannister AJ *et al.* Histone post-translational modifications – cause and consequence of genome function. *Nat. Rev. Genet*. 2022;**23**:563–80. https://doi.org/10.1038/s41576-022-00468-7

126. Tabar MS, Parsania C, Giardina C *et al.* Intrinsically disordered regions define unique protein interaction networks in CHD family remodelers. *FASEB J.* 2025;**39**:e70632. https://doi.org/10.1096/fj.202402808RR
127. Ramachandran S, Ahmad K, Henikoff S. Transcription and remodeling produce asymmetrically unwrapped nucleosomal intermediates. *Mol. Cell* 2017;**68**:1038–53. https://doi.org/10.1016/j.molcel.2017.11.015
128. Levendosky RF, Sabantsev A, Deindl S *et al.* The Chd1 chromatin remodeler shifts hexasomes unidirectionally. *eLife* 2016;**5**:e21356. https://doi.org/10.7554/eLife.21356
129. Hsieh LJ, Gourdet MA, Moore CM *et al.* A hexasome is the preferred substrate for the INO80 chromatin remodeling complex, allowing versatility of function. *Mol. Cell* 2022;**82**:2098–112. https://doi.org/10.1016/j.molcel.2022.04.026
130. Kato D, Osakabe A, Arimura Y *et al.* Crystal structure of the overlapping dinucleosome composed of hexasome and octasome. *Science* 2017;**356**:205–8. https://doi.org/10.1126/science.aak9867
131. Klein DC, Troy K, Tripplehorn SA *et al.* The esBAF and ISWI nucleosome remodeling complexes influence occupancy of overlapping dinucleosomes and fragile nucleosomes in murine embryonic stem cells. *BMC Genomics* 2023;**24**:201. https://doi.org/10.1186/s12864-023-09287-4
132. Liu Y, Warfield L, Zhang C *et al.* Phosphorylation of the transcription elongation factor Spt5 by yeast Bur1 kinase stimulates recruitment of the PAF complex. *Mol. Cell. Biol.* 2009;**29**:4852–63. https://doi.org/10.1128/MCB.00609-09
133. Zhou K, Kuo WH, Fillingham J *et al.* Control of transcriptional elongation and cotranscriptional histone modification by the yeast BUR kinase substrate Spt5. *Proc. Natl. Acad. Sci. USA* 2009;**106**:6956–61. https://doi.org/10.1073/pnas.0806302106
134. Farnung L, Ochmann M, Engeholm M *et al.* Structural basis of nucleosome transcription mediated by Chd1 and FACT. *Nat. Struct. Mol. Biol.* 2021;**28**:382–7. https://doi.org/10.1038/s41594-021-00578-6
135. Liu Y, Zhou K, Zhang N *et al.* FACT caught in the act of manipulating the nucleosome. *Nature* 2020;**577**:426–31. https://doi.org/10.1038/s41586-019-1820-0
136. Sims RJ 3rd, Millhouse S, Chen CF *et al.* Recognition of trimethylated histone H3 lysine 4 facilitates the recruitment of transcription postinitiation factors and pre-mRNA splicing. *Mol. Cell* 2007;**28**:665–76. https://doi.org/10.1016/j.molcel.2007.11.010
137. Skene PJ, Hernandez AE, Groudine M *et al.* The nucleosomal barrier to promoter escape by RNA polymerase II is overcome by the chromatin remodeler Chd1. *eLife* 2014;**3**:e02042. https://doi.org/10.7554/eLife.02042
138. Zhao D, Lu X, Wang G *et al.* Synthetic essentiality of chromatin remodelling factor CHD1 in PTEN-deficient cancer. *Nature* 2017;**542**:484–8. https://doi.org/10.1038/nature21357
139. Weiner A, Hughes A, Yassour M *et al.* High-resolution nucleosome mapping reveals transcription-dependent promoter packaging. *Genome Res.* 2010;**20**:90–100. https://doi.org/10.1101/gr.098509.109
140. Chen F, Liu B, Zeng J *et al.* Crystal structure of the core module of the yeast Paf1 complex. *J. Mol. Biol.* 2022;**434**:167369. https://doi.org/10.1016/j.jmb.2021.167369
141. Hainer SJ, Gu W, Carone BR *et al.* Suppression of pervasive noncoding transcription in embryonic stem cells by esBAF. *Genes Dev.* 2015;**29**:362–78. https://doi.org/10.1101/gad.253534.114

Received: December 4, 2024. **Revised:** July 18, 2025. **Editorial Decision:** August 2, 2025. **Accepted:** August 5, 2025